ADAR1 haploinsufficiency and sustained viral RdRp dsRNA synthesis synergize to dysregulate RNA editing and cause multi-system interferonopathy

Caitlin M. Miller[1,3], James H. Morrison[1,3], Laura Bankers[1], Rachael Dran[1], Julia M. Kendrick[1], Emma Briggs[2], Virginia L. Ferguson[2], and Eric M. Poeschla[1*]

[1]Division of Infectious Diseases, Anschutz Medical Campus, University of Colorado School of Medicine, Aurora, Colorado, USA 80045
[2]Department of Mechanical Engineering and BioFrontiers Institute, University of Colorado at Boulder, Boulder, CO, 80309
[3]These authors contributed equally
[*]Correspondence: eric.poeschla@cuanschutz.edu

SUMMARY

Sensing of viral double-stranded RNA by MDA5 triggers abundant but transient interferon-stimulated gene (ISGs) expression. If dsRNA synthesis is made persistent by transgenically expressing a picornaviral RNA-dependent RNA polymerase (RdRp) in mice, lifelong MDA5 activation and marked, global ISG upregulation result. This confers robust protection from viral diseases but in contrast to numerous other chronic MDA5 hyperactivation states, the mice suffer no autoimmune consequences. Here we find they further confound expectations by being resistant to a strong autoimmunity (lupus) provocation. However, knockout of one allele of *Adar*, which by itself is also well-tolerated, breaks the protective state and results in a severe disease that resembles interferonopathies caused by MDA5 gain-of-function mutations. In *Adar*$^{+/-}$ RdRp transgenic mice, A-to-I editing is both dysregulated and increased (numbers of genes and sites). This dsRNA-driven, MDA5-wild type model establishes that viral polymerase-sourced dsRNA can drive interferonopathy pathogenesis and illuminates the autoimmunity preventing role of ADAR1, while the ADAR1-intact viral RdRp model distinctively uncouples chronic MDA5 hyperactivity and autoinflammatory disease.

Keywords: ADAR1; MDA5; innate antiviral immunity; picornavirus; RdRp; autoimmunity; autoinflammation; interferonopathy; lupus

INTRODUCTION

Double-stranded RNA (dsRNA), a requisite intermediate during the replication of RNA viruses, is a pathogen-associated molecular pattern that induces an array of first-line antiviral defenses. Two specialized RNA helicases function as the main pattern recognition receptors (PRRs) that detect viral dsRNA: retinoic acid inducible gene-I (RIG-I) and melanoma differentiation antigen 5 (MDA5). Both of these RIG-I-like receptors (RLRs) are cytosolic sensors that signal through the adaptor MAVS, which instigates signaling cascades that eventuate in expression of numerous ISGs, either directly or via induction of secreted type I interferons (IFN-I).[1] RIG-I in general detects shorter or 5'-ppp containing dsRNAs and MDA5 detects the internal segments of longer (> 1 to 2 kb) dsRNAs.[2-4] A few RNA viruses are exclusively sensed by one RLR[1]. Picornaviral dsRNAs, for example, are detected by MDA5 and not RIG-I.[1,5-8]

The challenge such a system poses for the host is to securely differentiate viral dsRNAs from the vast, diverse pool of cellular RNAs, many of which can also harbor extended RNA duplex segments, particularly within retroelement-derived RNAs that are abundant in mammalian genomes.[9,10] Inappropriate or sustained activations of RLRs and other signaling pathways by endogenous nucleic acid ligands are associated with a variety of autoimmune diseases, which include classical, common syndromes such as systemic lupus erythematosus (SLE), type I diabetes mellitus, and psoriasis as well as various and frequently severe genetic conditions known collectively as interferonopathies. These auto-inflammatory conditions are characterized by persistent IFN-I and ISG expression and diverse end organ pathologies.[5,11,12]

The RNA modifying enzyme Adenosine Deaminase Acting on RNA 1 (ADAR1) has recently been identified as a central constraint on dsRNA-triggered autoimmunity.[13-17] Encoded by *ADAR*, ADAR1 catalyzes post-transcriptional editing of host RNAs by deaminating adenosine to inosine, thereby disrupting A-U base-paring and preventing formation of long uninterrupted RNA duplexes.[9,10,18,19] A-to-I editing most prominently prevents detection by MDA5 or protein kinase regulated by dsRNA (PKR) of endogenous retroelement transcripts and other dsRNAs, which averts inappropriate immune activation or translational shutoff.[9,10] Such editing of transcripts can also cause protein recoding,[17,20,21] although the vast majority of A-to-I edits in mammals are in non-coding regions.[22-25] Strikingly, physiologically essential A-to-I editing represents a very small fraction of the editome, and moreover most editing is unnecessary for murine homeostasis in the absence of MDA5.[26,27] Hereditary mutations in *ADAR*, as well as in other genes such as

TREX1, *SAMHD1*, *RNASEH2, RNU7, LSM11, and IFIH1* (MDA5) have been linked to the development of the rare congenital inflammatory disorder Aicardi-Goutières syndrome (AGS), which clinically mimics encephalopathies caused by *in utero*-acquired virus infections.[11,14,28-33] Homozygous *Adar* gene knockout is embryonic lethal in mice, causing mass apoptosis of fetal liver hematopoietic cells by embryonic day 11.5-12.5.[20,34] In contrast, *Adar*$^{+/-}$ mice are phenotypically normal and born at expected Mendelian ratios.[18] Early fetal demise of *Adar* $^{-/-}$ mice has been linked mechanistically to activation of the MDA5 pathway by dsRNA regions in cellular RNAs, chiefly repetitive elements, that are normally masked by A-I editing.[15,18,20,34,35]

Indeed, constitutive MDA5 activation has been repeatedly observed to cause autoimmune syndromes such as AGS in both mice and humans.[31,36] In distinctive counterpoint, we have shown in a mouse model that chronic, systemic MDA5 activation caused by viral polymerase-generated dsRNA, which causes marked, lifelong ISG upregulation, can be well-tolerated, even when it is also strongly protective against viral diseases.[37-39] The mice are transgenic for the RdRp of a neurovirulent mouse picornavirus (Theiler's murine encephalomyelitis virus, TMEV) expressed under transcriptional control of the non-selective ubiquitin C promoter, which causes chronic dsRNA-triggered innate immune activation.[37,38] Tissues of the RdRp transgenic mice (RdRp^{tg} mice; see first Methods section for nomenclature) express low levels of the polymerase, which templates on host RNAs to synthesize dsRNA. Elevated dsRNA is detected in RdRp^{tg} mouse tissues using the J1 anti-dsRNA antibody.[37] In addition, a catalytic center mutant of the TMEV RdRp lacked all ISG up-regulating activity.[37] RdRp^{tg} mice have global, high upregulations of ISGs and robust protection against ordinarily lethal challenges by a variety of RNA and DNA viruses, including Theiler's virus itself, EMCV, vesicular stomatitis virus, a DNA herpesvirus (pseudorabies virus), and Friend retrovirus.[37,38,40,41] The model is mouse strain-independent, with equivalent phenotypes in FVB/NJ, BALB/c and C57BL/6J mice.

RdRp$^{tg/-}$ and RdRp$^{tg/tg}$ mice develop normally, with onset of the major ISG expression profile shortly after birth.[39] The intriguing lack of deleterious effects from their chronically elevated ISGome differs strikingly from other constitutive MDA5 activation states.[36] Body size, morphology, organ histology and longevity are normal.[37-39] Crosses with *Ifih1*$^{-/-}$ mice showed that the sustained innate immune activation is strictly dependent on MDA5, which is congruent with MDA5 but not RIG-I being the sensor of picornaviral dsRNAs.[1,5-8] It is further dependent on the downstream adaptor MAVS, and the type I IFN receptor (IFNAR1) and is abolished by knockout of these genes.[37] Although type I IFNs are not detectably over-expressed in RdRp^{tg} mice

tissues, antibody-mediated blockade of the type I IFN receptor in adults terminates the ISG profile, indicating that some ongoing IFN-I signaling is required to sustain it.[39] *TLR3*, *IFNGR1* and *RAG1* knockout crosses also showed the ISG profile does not depend on TLR3, interferon gamma signaling or the adaptive immune system. As expected from the complete abrogation of ISG upregulation by *Ifih1* knockout, *Ddx58* knockout mouse crosses further confirmed no dependence on RIG-I (our unpublished data). Thus, the model is distinctive in that it represents a pure dsRNA-induced MDA5 hyperactivation state, and also one that is mediated through the wild type MDA5 sensor, and via "viral" dsRNA.

Prompted by the well-tolerated ISG elevations in this model, we here carried out experiments that demonstrate that RdRp^{tg} mice also resist induction of SLE in the BM12 lupus model, which we find is linked to increased quantities and effector function of regulatory T cells (T_{reg}). We show that introducing single *Adar* allele knockout – which, similar to RdRp transgenesis, produces no abnormalities by itself – breaks the RdRp^{tg} protective state, yielding a severe autoinflammatory disease. RdRp^{tg} mice lacking one *Adar* allele have stunted growth, gray fur, abnormal dental and skeletal structures, failure to thrive, highly dysregulated ISG expression, and abnormal A-to-I editing.

These results with a nucleic acid-triggered but MDA5-wild type model help to illuminate an essential axis between ADAR1 and MDA5 in the regulation of the mammalian innate immune response and implicate RNA virus polymerase-generated RNAs as possible ligands triggering autoimmunity, while the *Adar*-intact model uncouples antivirally protective sustained ISG activation and autoinflammatory disease.

RESULTS

RdRp^{tg} mice resist induction of SLE. Since picornaviral RdRp^{tg} mice do not exhibit apparent fitness "costs" of their chronic immune system activation,[37-39] an unanswered question is whether they may be more autoimmunity-prone like other constitutive MDA5 activation models.[36,42,43] To address this experimentally, we carried out a strong autoimmunity provocation by adopting the BM12 inducible SLE model, in which lupus is initiated by injection of splenocytes from MHC class II-mismatched mice.[44,45] Wild type (WT) and RdRp$^{tg/-}$ mice were injected with $1x10^8$ splenocytes isolated from BM12 mice or were control-injected with PBS and

evaluated for disease two weeks later. One of the clearest morphological changes in the BM12 model is splenomegaly, which results from germinal center expansion. Spleens were harvested and weighed before processing for flow cytometric analyses. As anticipated, we observed a significant increase in spleen size in WT mouse BM12 splenocyte recipients, indicative of lupus-like disease initiation (**Fig. 1A**). In contrast, RdRp^{tg} mouse BM12 splenocyte recipients had only minor, statistically non-significant increases in spleen size (**Fig. 1A**, $p = 0.126$ as compared with PBS-injected RdRp^{tg} mice).

We next examined cellular subsets in the spleen, specifically germinal center B cells and plasma B cells, which expand as they become activated to secrete anti-nuclear antibodies (ANAs), and T follicular helper (T_{fh}) cells, which provide antigenic stimulus in germinal center reactions.[46,47] For all three cell populations, WT mouse BM12 splenocyte recipients developed significant increases, indicative of ongoing germinal center reactions and increased antibody production (**Fig. 1B,C**). In contrast, and paralleling the spleen measurements, RdRp^{tg} mouse BM12 splenocyte recipients developed little to no increases in all three cellular populations. Significant increases over sham-treated animals were only seen in germinal center B cells (**Fig. 1B,C).** Minor changes in overall B cell and T cell populations were also observed, but none that account for the drastic differences in cellular subsets seen in WT BM12 splenocyte recipient animals (**Fig. S1A,B**).

To corroborate the results, we collected serum from splenocyte-recipients and control PBS recipients to measure production of ANAs, which are a hallmark of SLE and drive pathology in this model.[44,45] We measured ANAs against double-stranded DNA (dsDNA) and Smith antigen (SmAg), both of which are frequently observed in SLE patients and SLE mouse models[47,48] (**Fig. 1D**). Similar to the changes in cellular populations, there were significant increases in both of these autoantibodies in WT BM12 splenocyte recipients compared to the PBS recipient controls. In contrast, the RdRp^{tg} mouse BM12 splenocyte recipients produced less of both autoantibodies.

T_{reg} cell expansion. Our previous investigations did not reveal significant differences in immune cell subsets between WT and RdRp^{tg} mice.[38] Here we extended the studies to assess autoimmune suppressor cells, specifically regulatory T cells (T_{regs}), which are critical for maintaining immune-tissue homeostasis. Knockout of T_{regs} results in disseminated autoimmune disease followed by rapid organismal decline and death.[49,50] Here we measured T_{reg} cell subsets

in age-matched animals. There was a highly significant increase in T_{reg} cells in $RdRp^{tg/-}$ mice compared to WT and specifically an increase in mature, effector T_{regs} (**Fig. 1E**). T_{reg} cell expansion in $RdRp^{tg}$ mice may aid their tolerance to chronic innate immune activation.

The combined cellular and ANA data indicate that $RdRp^{tg}$ mice are better able to control disease induction after an autoimmune provocation than WT mice. This result is distinctive compared to other MDA5-pathway driven hyperimmune mice models, which have been shown to be equally or more susceptible to autoimmunity induction.[42,43]

Investigation of ADAR1. In addition to Treg cells, we suspected that mechanisms of protection at the intrinsic cellular level are likely to provide key regulation. Given its known role in preventing activation of the MDA5 pathway by double stranded segments of endogenously encoded RNAs, we hypothesized that ADAR1 may prevent adverse inflammatory sequelae in $RdRp^{tg}$ mice. First, we determined whether *Adar* expression is affected by RdRp genotype status. *Adar* encodes two functional isoforms, ADAR1 p150, which edits transcripts in the cytoplasm and is IFN-inducible, and constitutively expressed ADAR1 p110, which is generated by alternative splicing or by translation from the p150 mRNA by leaky internal ribosome scanning[51] and edits transcripts in the nucleus.[19,52,53] We observed no significant difference at either the mRNA or protein levels in expression of the p110 isoform in $RdRp^{tg}$ mice as compared to WT mice (**Fig. 2A,C**). In contrast, there was a marked increase in expression of the IFN-inducible p150 isoform (**Fig. 2B,C).** These results suggested that ADAR1 p150, itself an ISG, is upregulated in RdRp mice, perhaps helping to modulate the ISG activation in these animals.

We next knocked down *ADAR* expression in human lung epithelial cells (A549) in which we have engineered and validated inducible TMEV RdRp expression under the control of a doxycycline (dox) inducible promoter.[37] These cells broadly upregulate ISGs in response to RdRp induction in a pattern very similar to the $RdRp^{tg}$ mouse.[37] In two separate experiments, we achieved knockdowns of ADAR p110 and p150 isoforms (**Fig. 2D**). Dox induction of the RdRp after siRNA transfection led to over three $\log_{10}$ increases in mRNAs for two classical ISGs, *OAS* and *ISG15*, which were moderately accentuated by *ADAR* depletion in these short-term experiments (**Fig. 2E**). We therefore proceeded to generate mice with *Adar* gene knockouts.

***Adar* haploinsufficiency, by itself well-tolerated, causes multi-system disease in RdRp^{tg} mice.** As noted, by two weeks after birth, RdRp^{tg} mice develop high, sustained upregulations of many ISGs and subsequently tolerate them throughout their (normal) lifespans.[37,39] To determine whether ADAR1 is involved in the protection against deleterious effects of autoinflammation, *RdRp*$^{tg/tg}$ mice were crossed with *Adar*$^{+/-}$ mice. *RdRp*$^{tg/-}$ mice also have elevated ISGs, albeit with more variability in fold-induction than RdRp$^{tg/tg}$ mice (for example, see **Fig. 2B,C** for expression of the ISG Adar p150, and Painter et al[37]). Since in our hands and others *Adar*$^{+/-}$ mice have no phenotypic abnormalities, we did not anticipate a major effect in first-generation crosses even in the presence of an RdRp-mediated ISG response, since the F1 animals will retain a functional *Adar* allele.

However, that was not the outcome. First, there were major gross phenotypic differences between *RdRp*$^{tg/-}$ *Adar*$^{+/-}$ mice and littermate *RdRp*$^{tg/-}$ *Adar*$^{+/+}$ controls (**Fig. 3A-C**). The RdRp^{tg} mice lacking one *Adar* allele were significantly smaller in size (**Fig. 3A, B**), with gray instead of black fur (**Fig. 3A, C**). These features were equivalent in males and females (**Fig. 3A, C**). *RdRp*$^{tg/-}$ *Adar*$^{+/-}$ mice also have small, poorly developed, misshapen teeth (**Fig. 3C**). Runting was unrelated to the dental abnormalities, since suckling behavior was unaffected. In addition, the size evaluations were done at the time of weaning, and post-weaning mice were kept on a wet chow diet, which they were also observed to ingest equivalently. *Adar*$^{+/-}$ mice were normal in appearance as expected.

Because of these phenotypic differences, we carried out tissue dissections. Survival of the *RdRp*$^{tg/-}$*Adar*$^{+/-}$ mice began to fall significantly by 10 weeks after birth (**Fig. S2**), so these studies were done at 4-5 weeks. Soft viscera including heart, lungs, liver, spleen, intestines, kidney and brain were proportionately small but the organ morphologies were otherwise not different from WT mice. Histological analysis of tissue sections by a veterinary pathologist did not reveal evidence for tissue inflammation or other abnormalities (**Fig. 3D).** Since some MDA5-driven mouse autoimmune models manifest with kidney impairment, blood urea nitrogen (BUN) values were determined at 4-5 weeks of age. Mean BUN was slightly higher in RdRp^{tg} mice but was not in either *Adar*$^{+/-}$ group (**Fig. 3E**). We also measured serum ANAs and found no significant increases in anti-dsDNA antibodies (data not shown as levels for all animals were below the limit of assay detection) or anti-SmAg antibodies (**Fig. 3F**). In addition to the abnormal teeth (**Fig. 3C**), necropsy revealed thin, pale long bones suggesting decreased bone density. Bone frailty was also readily apparent during cervical dislocations, which subjectively required much

less force Similar dental and bone abnormalities can occur in Singleton-Merten Syndrome (SMS), a rare human autosomal dominant innate immune disorder consisting of musculoskeletal abnormalities (osteopenia, osteoporosis, skull thickening, small stature, ligament frailty), dental anomalies (poor, primarily anterior teeth formation), variable arterial calcification, inflammatory skin changes (psoriasis), and a characteristic facies (high anterior hair line, broadened forehead, asymmetric ptosis, smooth philtrum, and thin upper vermillion).[54,55] Genetic studies of individuals with SMS have revealed causation by a subset of single amino acid missense gain-of-function (GOF) mutations in MDA5 (R822Q, A489T, T331I/R), which cause constitutive activation.[56-60] There is inter-familial and intra-familial variation in syndromic manifestations, with partial penetrance evident in some kindreds[55] and overlap with Aicardi-Goutières syndrome has been reported.[58,59,61] Similarly, two families with atypical SMS lacking the dental abnormalities were found to have constitutively active single amino acid mutants of RIG-I rather than MDA5.[62]

As *RdRp*$^{tg/-}$ *Adar*$^{+/-}$ mice had micrognathia as well as small, misshapen and partially translucent incisors (**Fig. 3C**), µCT imaging and mechanical property assessments of femurs were performed to determine whether *RdRp*$^{tg/-}$ *Adar*$^{+/-}$ mice also had altered underlying changes to bone architecture or properties. Consistent with the runting observed in 5-week old mice (**Fig. 3A,B**), femurs of 6-week old *RdRp*$^{tg/-}$ *Adar*$^{+/-}$ were significantly shorter than control groups (**Fig. 4A,B**). As in other RLR-related genetic disorders[55,62], weight, femur length, and other mouse characteristics were variably penetrant. Bartlett's test demonstrated a statistically significant (p=0.0142) difference in homoscedasticity for femur length, yet a Kolmogorov-Smirnov test did not identify any significant (alpha=0.05) deviation from normal distribution for *RdRp*$^{tg/-}$ *Adar*$^{+/-}$ or other groups. Thus, we did not separate *RdRp*$^{tg/-}$ *Adar*$^{+/-}$ mice into 'penetrant' and 'non-penetrant' subsets in subsequent analyses and graphics, but we labeled mice with gray fur with light blue symbols in Fig. 4. *RdRp*$^{tg/-}$ *Adar*$^{+/-}$ femurs had significantly reduced cortical bone volume fraction and correspondingly reduced measures of cortical thickness, perimeter, area and porosity (**Fig. 4C**). In contrast, trabecular number and trabecular separation were not different between groups (**Fig. 4D-E**). Mechanical properties of the femurs were further investigated using three-point bending to failure. Stiffness and maximum load of *RdRp*$^{tg/-}$ *Adar*$^{+/-}$ femurs were significantly reduced compared to control groups (**Fig. 4F,G**). Modulus and ultimate stress of the femurs were calculated from mechanical properties and mid-diaphysis cross-sectional geometry from µCT. In contrast to the reduced mechanical properties observed, these material properties of *RdRp*$^{tg/-}$ *Adar*$^{+/-}$ femurs were not altered (**Fig. 4I-J**), nor was the total

cortical mineral density calculated from the µCT imaging (**Fig. 4H**). These results indicate that double heterozygosity (*RdRp*$^{tg/-}$ *Adar*$^{+/-}$) led to femurs having inferior stiffness and strength stemming from smaller size but not from impaired bone material quality, in addition to their dental mal-development and fur graying.

Resemblance to classical human SMS was partial since we the mice did not develop aortic or cardiac valvular calcification (**Fig. S3**), a core feature of the human syndrome, nor was there aberrant brain calcification (**Fig. S3**) as occurs in AGS[11] and in some SMS-AGS overlap cases[58,59,61]. Psoriasis is less commonly observed in SMS patients and was not observed in *RdRp*$^{tg/-}$ *Adar*$^{+/-}$ animals, leaving fur graying as the identifiable integument abnormality. Glaucoma can also occur in SMS, but intraocular pressures measured by tonometry in affected mice were normal and not significantly different from WT mice (data not shown).

Transcriptional changes in *RdRp*$^{tg/-}$ *Adar*$^{+/-}$ mice are consistent with an interferonopathy. The SMS-resembling phenotype triggered by the combination of one RdRp transgene allele and one *Adar* null allele, with neither alone producing abnormalities, prompted us to examine tissues further for differences that may be driving pathogenesis. We performed RNA-seq on brain tissue, with four biological replicates from each of the four genotypes WT, *Adar*$^{+/-}$, *RdRp*$^{tg/-}$ and *RdRp*$^{tg/-}$ *Adar*$^{+/-}$. Brains were analyzed because we previously observed that brains of RdRp^{tg} mice have particularly high ISG elevations compared to other organs, although gene expression changes are qualitatively similar and substantial across all major organs.[39] Here, in multidimensional scaling plots, we observed that the samples cluster strongly by genotype along the M1 axis, which validates that animals of the same genotype have similar gene expression profiles (**Fig. 5A**). The double heterozygotes (*RdRp*$^{tg/-}$ *Adar*$^{+/-}$) cluster the farthest from any other genotype, suggesting they have distinctly different RNA expression patterns. Assessing expression changes across the groups, the greatest differences were between *RdRp*$^{tg/-}$ *Adar*$^{+/-}$ mice relative to WT mice and relative to *Adar*$^{+/-}$ mice, with the majority of upregulated genes being known ISGs (136 out of 151 and 124 out of 137, respectively) (**Fig. 5B,C**). These outcomes suggest that *RdRp*$^{tg/-}$ *Adar*$^{+/-}$ mice have an extreme ISG response that likely leads to the Singleton-Merten interferonopathy-resembling phenotype. Interestingly, when we examined which genes are changing across genotype comparisons, we saw a largely overlapping set of ISGs upregulated in the presence of the RdRp transgene or in the absence of one *Adar* allele (**Fig. 5D**). All three non-WT genotypes (*Adar*$^{+/-}$, *RdRp*$^{tg/-}$, and *RdRp*$^{tg/-}$ *Adar*$^{+/-}$) showed significant upregulation of overlapping ISGs, but the magnitude of upregulation varies drastically by

genotype (**Fig. 5D**). Consistently the dual heterozygotes have extremely high induction, elevated 3-5-fold over what we observed in *RdRp*$^{tg/-}$ mice, while *Adar*$^{+/-}$ have only low level ISG induction (**Fig. 5D**). Thus, synergy between the RdRp transgene and the absence of one *Adar* allele leads to a hyper-induced ISG state in mice that is no longer tolerated.

Pathway Analysis. Ingenuity Pathway Analysis (IPA) was used to assess which canonical molecular pathways are activated or inhibited. *Adar*$^{+/-}$, *RdRp*$^{tg/-}$, and *RdRp*$^{tg/-}$ *Adar*$^{+/-}$ mice showed activation of genes related to interferon signaling, neuroinflammatory signaling and PRRs (**Fig. 5E**). Genes associated with dendritic cell (DC) maturation were activated in *RdRp*$^{tg/-}$ and *RdRp*$^{tg/-}$ *Adar*$^{+/-}$ mice (**Fig. 5E**). Increased DC maturation, specifically in *RdRp*$^{tg/-}$ *Adar*$^{+/-}$ animals, may contribute to the observed disease. We also carried out analyses of upstream regulators that may be responsible for gene expression patterns. In WT-*Adar*$^{+/-}$, *RdRp*$^{tg/-}$ *Adar*$^{+/+}$, and *RdRp*$^{tg/-}$ *Adar*$^{+/-}$ mice, we not surprisingly identified *Ddx58* (RIG-I), and *Ifih1* (MDA5) as upstream regulators activated in those samples (**Fig. S4**). Main intermediates in interferon signaling pathways, including IRF7, IRF9, STAT1, and STAT2 were also statistically significant predicted key regulators. (**Fig. S4**). Only in mice missing one *Adar* allele (*Adar*$^{+/-}$ and *RdRp*$^{tg/-}$ *Adar*$^{+/-}$ mice) did we also identify predicted regulation by additional PRR proteins, including TLR3, which recognizes dsRNA, and *ZBP1* (DAI), which recognizes Z-form nucleic acids,[63] both resulting in activation of interferon signaling (**Fig. S4**). Interactions with other nucleic acid sensing molecules besides MDA5 may thus play roles in sensing of ADAR1-edited transcripts.

Molecular and cellular differences in *RdRp*$^{tg/-}$ *Adar*$^{+/-}$ mice validate RNA-seq analyses and are consistent with interferonopathy. To characterize the RNA-seq results further, we determined levels of ISG mRNAs in brain tissues of *Adar*$^{+/+}$ and *Adar*$^{+/-}$ mice, with or without the RdRp transgene. Similar to the RNA-seq data, in *Adar*$^{+/-}$ mice, there were only small increases in levels of three classical ISG mRNAs compared to WT mice (about 2- to 5-fold; **Fig. 6A**). In contrast, and consistent with prior data,[37-39] *RdRp*$^{tg/-}$ mice had major increases compared to WT mice. However, the dual heterozygotes (*RdRp*$^{tg/-}$ *Adar*$^{+/-}$) had much higher ISG mRNA elevations, on the order of 200 – 600 fold relative to WT.

Importantly too, breeding to *Ifih1*$^{-/-}$ mice demonstrated that loss of MDA5 resulted in rescue of animal growth and a complete abolishment of ISG upregulation observed in *RdRp*$^{tg/-}$ *Adar*$^{+/-}$ animals (**Fig. S5**), reinforcing the MDA5-dependence of the phenotypes. Given the massively amplified ISG transcriptional pattern in the double heterozygotes, and the immune cell activation

and maturation pathways enrichment observed (**Fig. 5, Fig. S6**), we next harvested the spleens of 4-5 week old mice for flow cytometry analyses.

Aberrantly activated immune cell subsets are canonical autoimmune disease features and identifying them would support the conclusion of a dysregulated immune state in *RdRp*$^{tg/-}$ *Adar*$^{+/-}$ mice. In major immune cell populations in the spleens, including B cells, T cells, neutrophils, DCs, and granulocytes, we found no major differences in cell population proportions across different genotypes (**Fig. S7A**). The antiviral protein BST-2 (Tetherin) is a classical ISG with a high dynamic range of expression in response to type I interferon stimulation in multiple mammals, including mice,[64-66] and the mRNA was consistently upregulated across comparisons in the RNA-seq experiments. We therefore determined cell surface BST-2 protein expression in the various immune cell populations, and found it to be elevated on all cell types of *RdRp*$^{tg/-}$ *Adar*$^{+/-}$ mice and was slightly upregulated on DCs in WT-*Adar*$^{+/-}$ and *RdRp*$^{tg/-}$ animals and granulocytes from *RdRp*$^{tg/-}$ animals (**Fig. 6B**), similar to what we have observed previously.[38] We also examined monocyte and dendritic cell differentiation, maturation and activation in these animals (**Fig. 6C, D, E).** Monocytes were significantly increased in *RdRp*$^{t/-}$ *Adar*$^{+/-}$ animals (**Fig. 6C**) and cDC1s were slightly decreased also (**Fig. S7B**). Monocytes are circulating precursor cells that infiltrate into the tissue upon detection of proinflammatory stimuli and differentiate into effector monocyte-derived DCs (moDCs). An increase in this cell population is suggestive of increased demand for precursor cells in these animals. In support of this hypothesis, we observed increased BST-2 expression on all DC subsets from *RdRp*$^{tg/-}$ *Adar*$^{+/-}$ mice, as well as increased expression of the activation markers CD80/86 on *RdRp*$^{tg/-}$ *Adar*$^{+/-}$ monocytes and moDCs (**Fig. 6D, E**). Disorders in DC function and activity have been widely implicated in several autoimmune diseases, including SLE, and may contribute to disease development in *Adar*$^{+/-}$ RdRp$^{tg/-}$ animals.

Editome analyses show dual heterozygotes have dysregulated A-I editing. To interrogate the relationship of the loss of one *Adar* allele to the SMS-like phenotype of *RdRp*$^{tg/-}$ *Adar*$^{+/-}$ mice, we characterized genome-wide A-to-I editing differences between all four genotypes of animals (**Fig. 7**). We first carried out whole exome sequencing to eliminate any SNPs that may be unique to our colony or genotypes (of which very few were detected), as compared to the reference genome. We then identified all A-to-G changes in RNA-seq data (inosine is decoded as guanine during sequencing). We found that the majority of edited sites in all four genotypes were in intergenic regions and 3'UTRs, with a fractionally larger portion for 3'UTRs in RdRp^{tg}

mice. Exons and introns were represented approximately equivalently (**Fig. 7A, B**). Interestingly and unexpectedly, while edited site locations were similarly proportioned among the four genotypes (**Fig. 7A**), the number of edited sites increased substantially (50 – 65%) in *RdRp*$^{tg/-}$ *Adar*$^{+/-}$ mice compared to the other three genotypes (**Fig. 7B**). Numbers of edited genes also increased. This seemingly paradoxical result in the Singleton-Merten-affected dual heterozygotes was apparent across all gene regions. In contrast, in the *Adar*$^{+/-}$ and *RdRp*$^{tg/-}$ mice, the number of edited genes decreased compared to WT mice and the overall number of edited sites remained largely unchanged (**Fig. 7B**). Despite the number of edited sites being unchanged for WT, *Adar*$^{+/-}$, and *RdRp*$^{tg/-}$ mice, there was a shift from intergenic to extragenic regions in these animals, and there was a substantial proportionate rise in 3'UTR editing in RdRp$^{tg/-}$ mice of both genotypes, which was quantitatively greater in *RdRp*$^{tg/-}$ *Adar*$^{+/-}$ mice.

Because they possess only one functional *Adar* allele, it was unexpected that *RdRp*$^{tg/-}$ *Adar*$^{+/-}$ mice would have these increases in the number of A-to-I edited genes and A-to-I edited sites (**Fig. 7B**). Thus, there is a dysregulation of A-to-I editing. When we examined overlap of edited sites or edited genes between genotypes (visualized in Venn diagrams, **Fig. 7C**), we observed the highest number of uniquely edited genes (719) and sites (695) in *RdRp*$^{tg/-}$ *Adar*$^{+/-}$ mice, indicating that these animals have significantly different editing patterns compared to the other genotypes. It is notable that *RdRp*$^{tg/-}$ *Adar*$^{+/-}$ mice have increased editing in LINEs, SINEs, DNA transposons and other retrotransposons, since increases in retroelement transcription are associated with autoimmune disease states.[67] In addition, previous studies have shown ADAR1 to be critical for regulation of retroelement transcript self-reactivity[9,10] Increased ADAR-specific editing of retroelements is normally protective, but in our double heterozygote mice this alone is not compensatory enough to prevent disease, indicating that the A-to-I editing process in these animals is abnormal.

Next, we used RNA-seq to analyze the changes in edited genes, along with relative expression in each group of mice, to determine associations with activated/inhibited canonical pathways and enriched diseases and biological functions (**Fig. S8**). Of edited mRNAs in *RdRp*$^{tg/-}$ *Adar*$^{+/-}$ mice, genes associated with disease and biological functions related to apoptosis, cell death, and necrosis were enriched (**Fig. S8**). Notably, there was a clear reduction in genes involved in inflammatory disease states that was unique to comparisons with this *RdRp*$^{tg/-}$ *Adar*$^{+/-}$ mice (**Fig. S8**).

To explore the question further, we asked how A-to-I editing of ISG mRNAs, when it occurs, affects expression of their encoded proteins in *RdRp*$^{tg/-}$ *ADAR*$^{+/-}$ mice. We measured mRNA levels and performed protein immunoblotting for several ISGs that are uniquely edited in *RdRp*$^{tg/-}$ *Adar*$^{+/-}$ mice: Rig-I, Isg15, and Zbp1. Both Rig-I (*Ddx58*) and Zbp1 (*Zbp1*) were also predicted by the RNA-seq analysis to be key upstream gene regulators (genes with known activation/inhibition effects on the enriched pathways; **Fig. S4**). Expression levels of Rig-I, Isg15, and to a much lesser extent and not at the protein level, Zbp1, were increased in *RdRp*$^{tg/-}$ and *RdRp*$^{tg/-}$ *Adar*$^{+/-}$ mice, but not in *Adar*$^{+/-}$ mice (**Fig. 7D**,**E)** indicating that A-to-I editing does not reduce expression of these ISGs. Additionally, ADAR1 isoforms were expressed in *RdRp*$^{tg/-}$ *Adar*$^{+/-}$ mice at relatively similar levels as their *wild type* counterpart (**Fig. 7E,F**), with slightly higher p150 protein in *RdRp*$^{tg/-}$ mice and *RdRp*$^{tg/-}$*Adar*$^{+/-}$ mice. Notably, in *Adar*$^{+/-}$ mice alone, we observed decreased ADAR1 protein expression (**Fig. 7F**), as would be predicted from loss of an allele.

Endogenous retroelements are enriched in the 3' UTRs of ISG mRNAs.[68] Despite the increased ISG mRNA expression in *RdRp*$^{tg/-}$ *Adar*$^{+/-}$ animals compared to WT animals (Figure 5C), the proportion of uniquely edited sites that were within an ISG RNA versus those of other genes was not significantly elevated (**Fig. S9**). This was the case despite the double heterozygotes having an increase in total edited genes and sites (Figure 7C). Compared to the WT and double heterozygotes, *RdRp*$^{tg/-}$ and particularly *Adar*$^{+/-}$ animals had small, though significant, reductions in the proportion of uniquely edited sites falling within an ISG. These results suggest that while ISGs themselves were also edited, the amount of editing within the ISG mRNAs does not account for the observed dysregulation of Adar editing.

In summary, single *Adar* allelic loss coupled with transgenic expression of the picornavirus RdRp synergize to cause an extreme ISG response which produces an interferonopathy remarkably similar to Singleton-Merten syndrome. This work presents a novel model for this disease, which can be further studied to unlock molecular mechanisms driving the pathology. The ADAR-intact model is exceptional for its paradoxical combination of tolerated MDA5 hyperactivity with autoimmunity resistance.

DISCUSSION

Precise regulation of intracellular RNA duplex sensing is critical for protecting mammals against the Scylla of viral disease while also evading the Charybdis of autoimmunity. Confining sensing to only exogenous dsRNAs via PRRs such as MDA5 is therefore a bedrock feature of healthy antiviral defense. However, since MDA5 is relatively non-discriminating in its ligand preferences (mainly binding to internal segments of longer dsRNA duplexes on the order of hundreds to thousands of nucleotides in length), it has become clear in the past few years that an additional layer of control, ADAR1 p150 editing of host cellular RNAs, is at play. Nevertheless, the biological significance of the millions of A-to-I edits that modify RNA transcripts are incompletely understood.

In the same year in which he published his Nobel-awarded paper on the YF17D yellow fever vaccine that is still used today,[69] virologist Max Theiler reported his isolation of Theiler's virus and noted its similarities to poliovirus.[70] Here we identify new features of a mouse model in which we express the dsRNA-synthesizing enzyme of this picornavirus outside the viral context in the tissues of mice, providing a continuous dsRNA stimulus to the MDA5-MAVS pathway. In its strict MDA5-MAVS dependence, the model parallels the exclusively MDA5-dependent pattern for sensing of replicating picornaviruses.[1,5-8] Having previously demonstrated the lack of significant autoinflammatory cost to the animals, we found here that RdRp^{tg} mice are further able to resist an autoimmune provocation of induced SLE in the BM12 model (**Fig. 1**). However, the loss of a single *Adar* allele, which by itself is not discernibly harmful in our and others' hands,[18] breaks the autoinflammation-protected state, resulting in a severe disease characterized by extreme ISG elevations, dysregulated and increased A-to-I editing, bone and teeth abnormalities, stunted growth, and prematurely gray hair.

Among ADAR1 mouse models that produce autoinflammatory pathology, this is the only one with a simple haploinsufficient genotype and a wild type remaining *Adar* allele All others are either *Adar* $^{-/-}$ (which is embryonic lethal without an *Mda5* KO rescue) or utilize protein mutants such as *Adar*^{P95A} or *Adar*^{E861A} (see Rehwinkel and Mehdipour 2024[71] for a comprehensive list of existing mouse models). Relatedly, we further emphasize that the present model is nucleic acid-driven rather than MDA5 GOF mutation-triggered. As such it is a mouse model in which 'endogenously' synthesized RNAs generate an autoinflammatory disease via wild type MDA5, with the source of the dsRNA being a genomically-integrated viral polymerase. Since loss of

one *Adar* allele is enough to tilt the immune system in RdRp^{tg} mice to a highly pathogenic autoinflammatory outcome, it can be speculated that in some natural circumstances viral infections and the inflammatory signaling cascades they induce have roles in triggering human autoinflammatory diseases, particularly if they also disturb the finely regulated, complex equilibrium of A-to-I editing. The RdRp$^{tg/-}$ *Adar*$^{+/-}$ model complements ADAR1 mutant mouse AGS models, which differ in utilizing mutant ADAR1 proteins[72-74], and which do not incorporate a viral polymerase. The pathological outcome in *RdRp*$^{tg/-}$ *Adar*$^{+/-}$ mice is variably penetrant, with about half of mice severely affected, a feature that is common in human SMS kindreds[55,62] as well ADAR1 mutant protein mouse models of AGS.[24,73]

In some respects, the pathologies observed in *RdRp*$^{tg/-}$ *Adar*$^{+/-}$ mice resemble the human interferonopathy SMS, with notable exceptions, e.g., the lack of aortic and valvular calcification typically seen in the human syndrome.[54,55] In previous studies phenotypes resembling AGS/SMS were produced by engineering mice to express the MDA5 constitutive activation (GOF) mutants mG821S[75] or huR822Q.[76] In mG821S mice, SMS-like features were observed[75] but the model differs in that while it recapitulates skeletal defects, also seen in *RdRp*$^{tg/-}$ *Adar*$^{+/-}$ mice and human SMS cases,[56,57,59] it did not have the dental deformities or the fur pigmentation abnormality we observed, nor did we see the deteriorating kidney function found in mG821S mice. In the picornavirus RdRp^{tg} model, constitutive activation of WT MDA5 expressed from the endogenous locus by upstream provision of sustained dsRNA production is insufficient and addition of *Adar* haploinsufficiency is needed. It may thus have value as a model of nucleic acid-induced autoimmunity that reflects the overwhelming majority of patients, who have normal RLR proteins. In this regard, the G821S and R822W GOF MDA5 mutant proteins do not bind dsRNA and are always “on”. This may be central to the difference.

Why ADAR1, which mediates the most abundant form of RNA editing in Metazoan organisms,[77] does not edit RdRp-synthesized RNAs sufficiently to prevent activation of WT MDA5 in the RdRp^{tg} but *Adar*$^{+/+}$ mouse is unclear and is an intriguing aspect to investigate in the future. The data indicate that mammals have a means to prevent viral RdRp-synthesized dsRNA from being protected (from sensing) by A-to-I editing, even when the RdRp is expressed completely outside the context of actual viral replication, i.e., without the elaborate replication factory biogenesis central to the life cycles of all positive strand RNA viruses (and also without Vpg protein capping in the case of picornaviruses). How this occurs is a key topic for investigation in the field.

In prior reports of *Ifih1* gene duplication or mice carrying MDA5 GOF mutants, which also have increased expression of ISGs and relative protection against viral diseases, the mice have been shown to be more prone to either spontaneous or triggered autoimmunity.[36,42,43,75,76] Thus, RdRp^{tg} mice may have distinctive tolerance mechanisms as evidenced by their resistance to induced SLE. A component of these tolerance mechanisms may be the increase in overall and effector regulatory T cells (**Fig. 1**), which are key autoimmune suppressors cells.[49]

We conclude from our data that correctly regulated ADAR1 editing is a key suppressor of interferonopathic outcomes in these animals. The results also suggest that modulation of ADAR1 activity might potentially be of benefit in some human autoinflammatory diseases. Despite loss of one allele, ADAR1 levels, specifically the levels of ADAR p150 protein were increased equivalently in both *RdRp$^{tg/-}$* and *RdRp$^{tg/-}$ Adar+/-* animals, indicating that disease is not driven by a gene dosage effect in which low ADAR1 levels cause hypo-editing of dsRNA. Consistent with this result, a dysregulation picture emerged in which the overall number of edited sites and edited genes are increased in the double heterozygotes as compared to all other genotypes (**Fig. 7**). The dysregulation could contribute to the severe phenotype observed, but again, the comparison of the degree of p150 elevation with that of *RdRp$^{tg/-}$* mice compels an interpretation that the level of induced ADAR1 protein is not the main driver. For example, abnormally high levels of RNA editing have been reported in SLE patients.[78] When we measured the levels of proteins encoded by several uniquely edited ISG transcripts in *RdRp$^{tg/-}$ Adar$^{+/-}$* mice, we did not identify an effect of the additional edits. We considered whether increased ISG expression might lead to increased endogenous retroelement dsRNA expression, a possibility suggested by the observed increase in editing of SINES and LINES; in this regard, Zhang et al. showed that such endogenous retroelements are in fact quite enriched in the 3' UTRs of ISG mRNAs.[68] Here we found that multiple ISG mRNAS were indeed A-to-I edited but the proportion of uniquely edited sites that were within an ISG RNA versus those of other genes was not significantly elevated.

ADAR1 activity and editing changes in autoinflammatory diseases that are not directly linked to ADAR1 mutations are still poorly understood, but our data indicate that simple expression of the enzyme at physiological or higher levels does equate with proper function. It will be worthwhile to study changes in ADAR1 expression or dysregulation of A-to-I editing in interferonopathies and other autoimmune disease not directly linked to ADAR1.

In regard to the premature fur graying, dyschromatosis symmetrica hereditariais (DSH), a rare autosomal dominant skin pigmentation disorder, is associated with ADAR1 mutations in some human populations.[79] In these patients there is little correlation between genotype and phenotype, suggesting other genetic or environmental factors impact disease.[79] *Adar*$^{+/-}$ mice only develop the fur pigmentation abnormality in the presence of the RdRp transgene, suggesting a possibility that a second innate immune system trigger, such as exogenous viral activation of MDA5 signaling, could be involved in DSH. Rice et al. observed that *ADAR* haploinsufficiency or hypomorph function of missense variants are the probable molecular mechanisms in DSH.[14]

METHODS

Mice and nomenclature. RdRp transgenic mice on the C57/BL6J background have been previously described.[37] We here use *RdRp*$^{tg/-}$ to designate a mouse with one RdRp transgene allele and one normal locus lacking the chromosome 6 transgene insertion, *RdRp*$^{tg/tg}$ for transgene homozygotes, and RdRp^{tg}, without italics, for the general model. *Adar*$^{+/-}$ mice on the C57/BL6 background generated by Hartner et al.[20] were obtained from the Jackson Laboratory (MGI 3029789). There is a germline deletion of the gene region spanning exons 7-9, which results in non-functional p110 and p150 proteins.[20] Mice were backcrossed for two generations onto our colony before use and genotypes were confirmed using protocols suggested by the Jackson Laboratory. CD45.1^{+} congenic marker line mice were obtained from the Jackson Laboratory (mouse strain: 002014) and crossed onto the BM12 mouse line (Jackson Laboratory, 001162). Presence of the CD45.1 gene was confirmed via TransnetYX genotyping service (Ptprc-2 Mut probe) and confirmed with flow cytometric staining of splenocytes. BM12 genotyping was confirmed as described[45] in *Ifih1* knockout mice on a B6.J background were obtained from Jackson labs (strain 015812). As much as possible, littermate controls were used for direct comparison between groups. All experiments use a mix of male and female mice for analysis. All experiments were performed in accordance with the IACUC guidelines and approved procedures for the University of Colorado, Anschutz Medical Center (IACUC protocol no. 00116).

BM12 transfer. BM12 initiation of lupus like disease was done as described.[45] Briefly, $1x10^8$ splenocytes isolated from $CD45.1^+$ BM12 in mice were injected intraperitoneally into WT(CD45.2) or *RdRp*$^{tg/tg}$ (CD45.2) mice. Single cell solution in PBS or PSB alone (sham) was used for injection in 250 µL total volume. Mice were euthanized at 14 days post injection for disease evaluation.

Animal Imaging, µCT analysis, Intraocular pressure determinations. Femurs were evaluated for length, cortical bone structure and trabecular microarchitecture using a Zeiss Xradia Versa X-ray microscope-520 (µCT, Zeiss, Dublin, CA, USA; 80 kVp, 4x objective, isotropic voxel size of 4 µm). Regions of interest were located at the femur mid-diaphysis (1 mm tall) and the distal femur metaphysis (starting at 600 µm proximal to the epiphyseal line and extending 1,000 µm proximally). Trabecular and cortical bone were segmented and analyzed using Dragonfly Pro and Bone Analysis software (Object Research Systems, Montreal, Canada) according to established guidelines.[80] Trabecular bone parameters included bone volume fraction (Tb.BV/TV), trabecular number (Tb.N), trabecular thickness (Tb.Th), and trabecular separation (Tb.Sp). Cortical bone measures included cortical bone volume fraction (Ct.BV/TV), total bone mineral density (TMD), and cortical porosity (Ct.Po). The bending moments of inertia (Imax and Imin) which contribute to structural stiffness under bending were calculated. Hydrated femurs were evaluated using three-point bending to failure as described[81,82] to determine mechanical properties (e.g., stiffness and maximum load) using a MTS Insight II benchtop tester (MTS Corp., Minneapolis, MN; 250 N load cell, 5 mm/min deflection rate, 7 mm span width) and analyzed using custom MATLAB code, Mathworks, Natick, MA, USA). Material properties (e.g., modulus, ultimate stress) were calculated using standard equations derived from engineering beam theory.[81] Intraocular pressures were measured with a handheld ocular pneumotonometer (Model 30 Classic, Medtronic) as described.[83]

Cell culture and siRNA delivery. Triplicate biological replicates were used with three technical replicates each. A549 cell lines (ATTC, CCL-185) were maintained in Dulbecco's Modified Eagle's Medium (Corning) containing 10% fetal bovine serum and penicillin/streptomycin/L-glutamine (Corning, 100x solution). Doxycycline-inducible RdRp-expressing cells were described previously.[37] Two different siRNAs were used in combination for *ADAR* knockdown and were purchased from ThermoFisher Scientific (Catalog # 4390824, IDs s1008, s1009, previously validated). Negative control (ThermoFisher) or anti-*ADAR* siRNA were transfected into cells (50 pmol per well in a 6-well plate, cells seeded at >50% confluence) using

lipofectamine RNAimax reagent (ThermoFisher) according to manufacturer instructions. Cells were washed 6 hours post transfection and dox (2 µg/mL) was added at this time. At 48 hours post dox addition, cells were lysed for protein and RNA analysis.

Western blotting. Western blotting was done as previously described.[37,39] Briefly, cells were homogenized in RIPA buffer and protein content was determined by Bradford reaction (Bio-Rad). 30 µg total protein was loaded per well prepared in 6X reducing SDS sample buffer (Bio-Rad, boil for 5-10 minutes prior to loading). Samples were run on 10% agarose gels (Bio-Rad) and transferred to polyvinylidene difluoride membrane (Bio-Rad). Samples were blocked in 5% milk in tris-buffered saline containing 0.1% Tween20 (TBS-T). For human cell line derived blots, rabbit polyclonal anti-ADAR1 (1:1,000 dilution; Cell Signaling, 14175) primary antibody or mouse anti-tubulin (1:5,000 dilution; Sigma, T5168) were used. For mouse tissue blots, rabbit anti-Rig-I (1:1,000 dilution, Cell Signaling, 3743), mouse anti-ADAR1 (1:500 dilution, Santa Cruz Bio, sc-73408), rabbit anti-actin (1:5,000 dilution, Cell Signaling, 4967) or the previously described tubulin antibody was used. For detection, goat anti-rabbit secondary antibody conjugated to horseradish peroxidase (1:5,000 dilution; Calbiochem, 401393) or goat anti-mouse secondary antibody conjugated to horseradish peroxidase (1:5,000 dilution; Invitrogen, 31430) were used for all proteins of interest. Immobilon Crescendo Western HRP substrate (Millipore) was used for visualization of bands and imaged on a ChemiDoc XRS+ Imaging System (Bio-Rad).

Bioinformatics and Computational Methods. We used a combination of RNA sequencing and exome sequencing to evaluate transcriptome-wide patterns of RNA gene expression and ADAR-mediated A-to-I RNA editing. Specifically, we sequenced four biological replicates from each of the four genotypes for RNA-seq (WT-*Adar*$^{+/+}$, WT-*Adar*$^{+/-}$, *RdRp*$^{tg/-}$ *Adar*$^{+/+}$, and *RdRp*$^{tg/-}$ *Adar*$^{+/-}$) and a single sample from each genotype for exome sequencing. Exome sequencing was used to establish a baseline level of germline genetic variation within our mouse colony and was used as background for identifying RNA-edited sites. Library preparation and sequencing for single-end RNA-sequencing and paired-end exome sequencing were performed by BGI (Beijing Genomics Institute). The quality of raw reads was assessed using FASTQC v.0.11.5. We used Trimmomatic v.0.27 to filter out low quality reads that had a mean Phred quality score less than 20. Read quality was then reassessed with FASTQC. We used Hisat2 v.2.1.0 to map reads to the mm10 genome using default single-end parameters for RNA-seq and included the --no-mixed --no-discordant flags for the paired-end exome sequencing. Next we used Samtools

v.1.3.1 to convert the sam output files into bam format. Then we used PicardTools v.1.119 to add read groups, remove PCR duplicates, and coordinate sort the bam files. To evaluate RNA-seq gene expression patterns across the four genotypes, we first used Stringtie v.1.3.6 to quantify transcripts abundance, and Stringmerge to merge the output Stringtie GTF files. CuffDiff2 was to identify significantly differentially expressed genes (DEGs) with an FDR of 0.05 and Benjamini-Hochberg multiple test correction. In order to reduce false positives, we also required fragments per kilobase per million reads mapped (FPKM) to be at least four, and at 2-fold differences in expression because of the massive gene expression differences observed in[37,39] We used CummeRbund and Plotly to visualize our results. The Interferome Database was used to identify which DEGs were known ISGs. Finally, we used the Canonical Pathways and Diseases and Biological Functions analyses in IPA to determine which molecular pathways and biological functions were enriched among our conditions and to predict whether they were likely to be activated or inhibited based on gene expression patterns in our dataset. To identify RNA-edited sites, we used REDItools to call SNPs that were present in the RNA-seq, but not present in the exome sequencing. Because the A-to-I editing performed by ADAR is incorporated as A-to-G changes by sequencers, we looked for differences in A-to-G changes across conditions. We required a minimum of 10x coverage and that each putative RNA-editing SNP be sequenced at least twice to reduce the risk of including sequencing errors. First, we used Samtools mpileup to call SNPs in the exome sequencing data. We used REDItoolsDeNovo to call SNPs A-to-I edited sites in the RNA-seq requiring at least 10x coverage and that each SNP was sequenced at least twice. Putative germline SNPs identified in the exome sequencing were subtracted from the RNA SNPs. The resulting SNP tables were converted into bed format and sorted by coordinates using BedTools and we filtered SNPs to those present in all four biological replicates. We then annotated the SNPs using Homer annotatePeaks.pl to determine the genomic features in which SNPs occur. A-to-I editing patterns were compared across the four genotypes in two ways and visualized using SUMO, 1) whether editing occurred in the same vs. different genomic features, allowing editing sites to occur at different locations within that feature, and 2) whether editing occurred at identical sites. Finally, we used IPA to identify significantly enriched molecular pathways and biological functions associated with edited genes among the 4 genotypes.

Quantitative PCR. For qPCR analysis of mouse samples, RNA was extracted from mouse tissue using Trizol reagent (Ambion) according to manufacturer instructions. Reverse transcription PCR (RT-PCR) for cDNA synthesis was conducted using Maxima H Minus First Strand cDNA Synthesis Kit (Thermo Scientific) following manufacturer instructions. QPCR

analysis for quantification of cellular transcripts was done using 2X qPCR Green Master Mix (APEX) with the following primers for mice: 5'-CATGGCCTTCCGTGTTCCTA-3' and 5'-CTATGTTTCCCGCGGCACGTCAGATCCA-3' for Gapdh; 5'-TTTGTTGTTGTTGTTGTTCGTT-3' and 5'-GCAGGAATCAGTTGTGATCT-3' for Ifit1; 5'- TGGTACAGAACTGCAGCGAG -3' and 5'- CAGCCAGAACTGGTCTTCGT -3' for Isg15; and 5'-CAAACAAACAAACAAACCCTCTC-3' and 5'-TCAAGGTGTCACTCTGCAT-3' for Oasl2; 5'-GGTGGAAGACTACGCGTTGGGAC-3' and 5'-ACGACTGTGTCTGGTGAGGGAACAC-3' for ADARp110; 5'-GGCCTTGCCGGCACTATGTCTC-3' and 5'-GCGGGTATCTCCACTTGCTATGCTC-3' for ADARp150; and 5'-CACAGCCCTCTCCATCAACTATAAGCAG-3' and 5'-CTGTAGGTGAGGTTGATCTTTCCATTCAG-3' for IFNβ. For qPCR analysis from human cell lines, RNA extractions were done using an RNAeasy kit (Qiagen) according to kit protocol. RT- and qPCR were performed as described above with the following human primers: 5'-TGGACCTGACCTGCCGT-3' and 5'-TGGAGGAGTGGGTGTCGC-3' for GAPDH; 5'-GTGGACAAATGCGACGAACC-3' and 5'-ATTTCCGGCCCTTGATCCTG-3' for ISG15; and 5'-GGATCTTCTCCCACACTCACATCT-3' and 5'-CACCATCAGGATTCTTCACGAA-3' for OASL. Transcripts were quantified using the $\Delta\Delta C_T$ method relative to *Gapdh* or β-Actin (*Actb*) transcripts.

Flow Cytometry. Mice were euthanized by CO_2 asphyxiation and subsequent cardiac puncture. Spleens were excised and placed in 15 mL conical tubes containing 3 mL of DMEM containing FBS and antibiotics. Spleen was manually dissociated with a pipette tip and pipetting, then passed through a 40 µM nylon cell strainer. 100 µL from each sample were combined and used for the isotype and unstained controls. Cells were gated to exclude debris, doublets, and dead cells based on viability dye staining. Cell population abundance: samples had at least 1x10^6 cells sorted in the live population and cell types are shown as percent of live cells for all flow cytometry data. Each cell type described had a minimum of about 0.5% meaning all cell types described were observed at a frequency of about 5,000 or more per sample. Analysis of cellular populations was conducted as previously described[38]. Gating strategies are shown in **Figs. S10-13**. For staining of splenocyte populations, cells were red blood cell depleted as described.[38] For analysis including FoxP3 staining, intracellular transcription factor staining was done using Foxp3/Transcription Factor Staining Buffer Set (eBioscience) according to manufacturer instructions for use in a 96-well plate. DC-specific staining panel has been previously described.[38] T_{reg} staining panel consists of the following antibodies/cellular stains: fixable viability dye eFlour780 (eBioscience, 65-0865-14), PE anti-mouse FoxP3 (BioLegend,

126404), PerCP-Cy5.5 anti-mouse CD4 (BioLegend, 100434), Brilliant Violet 421 anti-mouse CD25 (BioLegend, 101923), APC anti-mouse CTLA-4 (BioLegend, 106310), Brilliant Violet 711 anti-mouse GITR (BD Bioscience, 563390), Brilliant Violet 605 anti-mouse ICOS (BioLegend, 313538), Brilliant Violet 480 anti-mouse CD44 (BD Bioscience, 566116) and FITC anti-mouse CD62L (BioLegend, 104406). For analysis of B cells (germinal center and plasmablast) the following antibodies and cellular stains were used: fixable viability dye eFlour780 (eBioscience, 65-0865-14), Brilliant Violet 421 anti-mouse CD138 (BioLegend, 142507), PE anti-mouse Fas (BD Bioscience, 554258), Alexa Fluor 488 anti-mouse GL-7 (BioLegend, 144612). For T_{FH} cell analysis and CD45.1 engraftment, the following antibodies and cellular stains were used: fixable viability dye eFlour780 (eBioscience, 65-0865-14), PerCP-Cy5.5 anti-mouse CD4 (BioLegend, 100434), Brilliant Violett 711 anti-mouse TCRβ (BioLegend, 109243), PE anti-mouse PD-1 (BioLegend, 135205), APC anti-mouse CXCR5 (BioLegend, 145506), and Brilliant Violet 421 anti-mouse CD45.1 (BioLegend, 110732). BST-2 was detected with Pacific Blue anti-mouse BST-2 (BioLegend, 127108). Gating for B cell and T_{FH} cell analysis was described in ref[45]. Isotype staining for each panel was done in parallel. Gating was set based on fluorescence minus one controls. Cells were gated to exclude debris, doublets, and dead cells based on viability dye staining. Gating for DC-subtype determination was described in ref[38]. All data was acquired on an LSRII (BD Biosciences) and analysis was done using FlowJo software.

ELISAs. Mouse serum was used for ANA detection via ELISA. For detection of anti-dsDNA antibodies, calf thymus DNA (Sigma, D4522) was digested with S1 nuclease (ThermoFisher, EN0321) to remove any single stranded DNA (ssDNA). DNA was ethanol precipitated and resuspended in nuclease free water. Freeze-thaw cycles were avoided to prevent creation of new ssDNA. Nunc MaxiSorp ELISA plates (Sigma) were coated with Poly-L Lysine (0.01% final, Millipore Sigma) prior to use. Plates were coated overnight with dsDNA (3 µg/mL) in PBS at room temperature and blocked with BSA in PBS (3% final, Sigma). For a standard, anti-dsDNA (Abcam, ab27156) was used between the range of 1 µg/mL – 1.37 ng/mL (3-fold dilutions) and serum samples were initially diluted 1:10 and then as needed. For anti-smAg ELISAs, plates were coated with Sm Ag (3 µg/mL, Genway Biotech, GWB-CA4A65) in PBS overnight. Blocking was done in 1% BSA/PBS. For standard, anti-SmAg (Novus Biologicals, NB600-546) was used between the range of 1 µg/mL – 15.63 ng/mL (2-fold dilutions) and serum samples were diluted 1:10 before use and then as needed. For both ELISAs, standard and serum samples were diluted in sample buffer (0.5% Tween20, 1% BSA in PBS) and plates were washed 3-5 times between incubations with wash solution (0.5% Tween20 in PBS). Plates were incubated with

samples/standard for 2 hours at 37°C. Detection antibody used was goat anti-mouse IgG peroxidase (1:10,000 dilution; Sigma, A2554) and peroxidase was developed used TMB ELISA HRP Substrate kit (Seracare) and Sulfuric acid (4N, Fisher Scientific) according to manufacturer instructions.

Calcium Quantification. Whole-brain tissue was flash frozen at necropsy, homogenized by sonication on ice in 4x volumes of calcium assay buffer (Calcium Assay Kit, Abcam ab102505), and free Ca^{2+} ions were quantified following the manufacturer's methods.

Histology. Briefly, approximately 2 cm thick tissue sections were fixed in 10% formalin for 24 hours then washed twice and suspended in 70% ethanol. Tissues were paraffin embedded, cut and stained for Alizarin Red or H&E by our Research Histology Core Laboratory. Pathological analysis and scoring was done by a certified pathologist (IDEXX BioAnalytics).

Data availability

The data and associated protocols that support the findings of this study are available from the corresponding author upon request. The RNA-seq and whole exome sequencing datasets have been deposited to the NCBI sequence read archive (SRA SUB14698103).

Inclusion and Ethics Statement

This work did not involve human subjects, or samples or materials from other countries, nor are data from third parties included. All animal experiments were performed humanely in accordance with the IACUC guidelines and approved procedures (IACUC protocol no. 00116) for the University of Colorado School of Medicine.

ACKNOWLDEGMENTS

Funding was provided by National Institutes of Health Avant-Garde grant DP1DA043915 (E.M.P.), a John H. Tietze Foundation grant (E.M.P.), and an NSF grant 1707065 (V.L.F.). We thank C. Radomile and J. Chen for technical assistance with animal experiments, the University of Colorado Denver School of Medicine (UCDSOM) Division of Allergy and Clinical Immunology Flow Cytometry Core for use of the LSRII instrument, the UCDSOM Research Histology Core Laboratory for tissue processing (RRID: SCR_021994), and the CU at Boulder Materials Instrumentation and Multimodal Imaging Core Facility (RRID: SCR_019307) for X-ray microscopy and micro-computed tomography imaging.

AUTHOR CONTRIBUTIONS

C.M.M. and J.H.M. conceived, designed and performed experiments, analyzed data and conducted statistical analysis and helped write the manuscript. L.B. performed RNA-seq and editome analysis and statistics and drafted related manuscript sections. R.D. performed experiments and managed the mouse colony. V.F. and E.B. contributed skeletal morphometry and imaging data and analysis and helped write the related manuscript sections. E.M.P. conceived, designed, and directed the project, assisted in plasmid cloning, and wrote the manuscript, with review and input from all authors during revisions.

Figure Legends

Figure 1. RdRp^{tg} mice resist SLE-like disease induction in the BM12 model of lupus. Ten-week-old mice were challenged with 100 million BM12-derived splenocytes. Mice were harvested 14 days post challenge for analyses. **(A)** Splenomegaly. Weights of BM12 and sham-injected mice spleens were measured. **(B,C)** Germinal center B cells, plasma cells and Tfh cells. RBC-lysed, single cell suspensions of splenocytes from BM12 or sham injected animals were generated for flow staining and germinal center B cells and plasma B cells (B), or follicular helper cell populations (C) were measured by flow cytometry according to gating described in materials and methods section. **(D)** Anti-nuclear antibodies. Sera from BM12 splenocyte-injected or sham injected mice were used to measure anti-dsDNA antibodies and anti-SmAg antibodies by quantitative ELISA. Data in A-D are from n = 7, 6, 8, 8 mice for WT (PBS), *RdRp$^{tg/-}$* (PBS), WT (BM12), and *RdRp$^{tg/-}$* (BM12) groups respectively. **(E)** T_{reg} cells. RBC-lysed single cell suspensions were generated from spleens of untreated, ten-week-old WT or RdRp^{tg} mice (n = 5 for each group) and T_{reg} subsets were determined by flow cytometry. Data were analyzed using one-way ANOVA followed by Tukey tests for (A-D) and an unpaired student's T test for (E). * = $p < 0.05$, ** = $p < 0.01$, *** = $p < 0.001$, **** = $p < 0.0001$. Data points represent individual animals, graphs show means with standard deviations (s.d.).

Figure 2. ADAR p150 and ADAR p110 levels in RdRp^{tg} mice, and effects of *ADAR* knockdown on RdRp-dependent ISG expression. RNA isolated from brains of 4 to 5 week old WT or *RdRp$^{tg/-}$* mice (n = 5 for WT, 6 for *RdRp$^{tg/-}$*) was used to measure **(A)** ADAR p110 and **(B)** ADAR p150 transcripts by qPCR. Data points represent individual animals, graphs shown means, s.d. **(C)** Immunoblotting for ADAR p110 and ADAR p150 in 4 to 5 week old mouse WT and *RdRp$^{tg/-}$* brain. **** = $p < 0.0001$; n = 3 animals per genotype. **(D)** A549 cells with inducible Theiler's virus RdRp (Tet-on system). Data are shown from two representative knockdowns. **(E)** RNAs isolated from the parallel knockdowns done in panel D were used for qPCR analysis to determine relative levels of the ISGs *OAS* and *ISG15* mRNAs. mRNAs were harvested 54 hours after *ADAR*-targeting siRNA addition and 48 hours after dox addition. Comparisons were made between dox-treated and dox-untreated cells and expressed as fold mRNA changes induced by dox. Transfection controls (cells receiving transfection reagents but no siRNA) showed similar levels of ISG induction after dox treatment as control siRNA-transfected cells, indicating lack of contribution of transfected siRNAs to immune activation. Data are means and s.d. of triplicate

biological replicates with three technical replicates each. NS: not significant; unpaired Student's T test.

Figure 3. Phenotypic and histological differences in RdRp$^{tg/-}$ Adar$^{+/-}$ mice. (A) Size and coat color differences in 5-week-old, littermate *RdRp$^{tg/-}$* and *RdRp$^{tg/-}$ Adar$^{+/-}$* mice. **(B)** Weight differences between 4 week and 5-week-old littermate *RdRp$^{tg/-}$* and *RdRp$^{tg/-}$ Adar$^{+/-}$* mice (n = 9 and 5 respectively). **(C)** Dental formation changes between *RdRp$^{tg/-}$* and *RdRp$^{tg/-}$ Adar$^{+/-}$* mice. **(D)** H & E-stained tissue sections from kidney, brain, lung, liver, heart and spleens from *RdRp$^{tg/-}$* and *RdRp$^{tg/-}$ Adar$^{+/-}$* littermate mice. Pathological grading revealed no significant scoring in *RdRp$^{tg/-}$ Adar$^{+/-}$* animals. **(E)** Blood Urea nitrogen from serum from 4-5 week old animals in WT, *Adar$^{+/-}$*, *RdRp$^{tg/-}$*, *Adar$^{+/-}$ RdRp$^{tg/-}$* mice. n = 5, 6, 5, 8 for WT, *Adar$^{+/-}$*, *RdRp$^{tg/-}$*, *Adar$^{+/-}$ RdRp$^{tg/-}$*, respectively. **(F)** Anti-SmAG antibodies from serum from 4-5 week old animals as measured by quantitative ELISA. Four outlier high values were seen, but two were in the WT group. n = 15, 7, 10, 9 for WT, *Adar$^{+/-}$*, *RdRp$^{tg/-}$*, *Adar$^{+/-}$ RdRp$^{tg/-}$*, respectively. Anti-dsDNA antibody levels from matched serum was below the limit of detection for all animals tested. Where not indicated, all data and tissue sections come from a mix of male and female mice. Data in (B) was analyzed by two-way ANOVA where ****$p < 0.0001$. Data in (E) and (F) were analyzed by one-way ANOVA where *$p < 0.05$; data points represent individual animals, graphs show means and s.d.

Figure 4: Skeletal and dental features of wild type, *RdRp$^{tg/-}$*, *Adar$^{+/-}$*, and *Adar$^{+/-}$ RdRp$^{tg/-}$* mice. Femurs from 6-week-old animals were manually de-fleshed and used for all analyses. **(A)** Femur lengths of WT, *Adar$^{+/-}$*, *RdRp$^{tg/-}$*, and *RdRp$^{tg/-}$ Adar$^{+/-}$* mice (n = 8, 6, 10, and 17 animals respectively). **(B)** Representative µCT images, distal femur sections and whole bone. **(C)** Cortical bone volume fraction (BV/TV), n = 8, 7, 10, 17. **(D)** Trabecular number, n = 8, 7, 9, 17. **(E)** Trabecular separation, n = 8, 7, 9, 17. **(F)** Stiffness, n = 8, 7, 10, 15. **(G)** Maximum load, n = 8, 7, 10, 17. **(H)** Cortical total mineral density, n = 8, 7, 10, 17. **(I)** Modulus, n = 8, 7, 10, 17. **(J)** Ultimate stress, n = 8, 7, 10, 17. Mice with gray fur are indicated by light-blue symbols. Data were analyzed first by using a ROUT test to remove outliers (Q = 1%), which resulted in removal of two mice from one group in one panel (the *RdRp$^{tg/-}$ Adar$^{+/-}$* group in Fig. 4F, stiffness testing; hence there are 15 mice as opposed to the 17 for this genotype in the other panels). A one-way ANOVA comparing *RdRp$^{tg/-}$ Adar$^{+/-}$* to each other group was used followed by a Tukey tests where * = $p < 0.05$, ** = $p < 0.01$, *** = $p < 0.001$, **** = $p < 0.0001$. Data points represent individual animals, horizontal bars indicate means.

Figure 5. RNA-seq analysis reveals clear pattern of ISG upregulation suggestive of an interferonopathy. RNA-seq from neuronal tissue from n = 4 age-matched (5 weeks) mice per group. Where possible, littermate controls were used for analysis. Two male and two female mice were used per group. **(A)** Multi-dimensional scaling plot of RNA expression profiles in WT-WT, *Adar*$^{+/-}$, *RdRp*$^{tg/-}$, and *RdRp*$^{tg/-}$ *Adar*$^{+/-}$ mice. **(B)** Heatmap of differentially expressed ISGs across the four genotypes. FPKM values were log transformed with 1 pseudocount to facilitate visualization. **(C)** Summary table of differentially expressed genes (DEGs) and proportions of which are known ISGs as determined by the Interferome database. **(D)** Differentially expressed genes that are shared across all group comparisons. **(E)** Canonical molecular pathways from IPA that are significant across group comparisons.

Figure 6. ISG and leukocyte subset differences in RdRp$^{tg/-}$ Adar$^{+/-}$ mice. (A) qPCR of three representative ISGs (*Ifit1*, *Isg15*, and *Oasl2*) in brain tissue of 4-5 week old WT, *Adar*$^{+/-}$, *RdRp*$^{tg/}$, and *RdRp*$^{tg/-}$ *Adar*$^{+/-}$ mice (n = 5, 5, 6, 5, respectively). **(B-E)** Flow cytometry analysis of cellular populations derived from the spleens of 4-5 week old mice. Single cell, RBC-lysed solutions were prepared for use in analysis. **(B)** BST-2 expression on the main immune cell subsets in the spleen including T cells (CD3^{+}), B cells (CD19^{+}), DCs (CD11c^{+}), granulocytes (Ly6G^{+}), and NK cells (NKp46^{+}). n = 7, 7, 4, 4 for WT, *Adar*$^{+/-}$, *RdRp*$^{tg/}$, *RdRp*$^{tg/-}$ *Adar*$^{+/-}$, respectively. **(C)** Monocytes populations across all four groups. **(D)** BST-2 expression on monocyte/DC cell subsets including monocytes, cDC1s, cDC2s, and moDCs. **(D)** Activation (CD80/86 expression) of monocyte/DC subsets including monocytes, cDC1s, cDC2s, and moDCs. C-E: n = 12, 7, 10, 8 for WT, *Adar*$^{+/-}$, *RdRp*$^{tg/}$, *RdRp*$^{tg/-}$ *Adar*$^{+/-}$, respectively. For all graphs shown, data were analyzed using a one-way ANOVA followed by a Tukey tests to determine significance where * = $p < 0.05$, ** = $p < 0.01$, *** = $p < 0.001$, **** = $p < 0.0001$. Data points represent individual animals with the mean and s.d. shown as bars.

Figure 7: Analysis of the A-to-I editome reveals increased editing in *RdRp*$^{tg/-}$ *Adar*$^{+/-}$ mice. Changes in A-to-I edits were determined via comparison of RNA-seq data with whole exome DNA sequencing. **(A)** Pie charts showing the proportion of editing sites within a given RNA element for each mouse genotype. **(B)** Table summary of the distribution of overall numbers of edited genes and sites for each genotype and the breakdown of locations of the edit sites among different RNA elements. For each of the four genotypes, four animals were sequenced and to be counted a gene must have been edited in all four animals sequenced but editing can occur anywhere in the gene. For sites, identical sites must be edited in all four animals of a

genotype. **(C)** Venn diagrams showing overlap of edited genes (top) or sites (bottom) among the four genotypes. **(D,E)** Immunoblot analysis from two animals per group (D) and gene expression fold change (E) of three *Adar*$^{+/-}$ *RdRp*$^{tg/-}$ uniquely edited genes in the RNA-seq data set (as compared to WT) in 5-week-old neuronal tissue. Rig-I, Isg15, and Zbp1 were evaluated as they are each ISGs that are highly upregulated in mice expressing RdRp and are key regulators of the antiviral response. **(F)** Expression of *Adar* isoforms in neuronal tissue of 4-5 week old mice from all four genotypes, as determined by western blot (n = 2 per group).

Supplemental Figure Legends

Figure S1: Overall B cell and T cell populations are marginally changed during BM12 transfer. Single cell, RBC-lysed splenocyte suspensions were made from sham or BM12 transferred animals for flow cytometry analysis. **(A)** Overall B cell populations in animals as defined by cd19 expression. **(B)** Overall $CD4^+$ T cell population in the spleens of experimental animals, as defined by TCRβ and CD4 expression. Data were analyzed using a one-way ANOVA followed by a Tukey tests where * = $p < 0.05$, ** = $p < 0.01$, *** = $p < 0.001$, **** = $p < 0.0001$. n = 7, 6, 8, 8 for WT (PBS), *RdRp*$^{tg/-}$ (PBS), WT (BM12), and *RdRp*$^{tg/-}$ (BM12), respectively. Data represent individual animals with the mean and s.d. shown as bars.

Figure S2: Reduced survival of *Adar*$^{+/-}$ *RdRp*$^{tg/-}$ mice. Survival of animals from each group was followed for 20 weeks and shown as a Kaplan-Meier plot. Data were analyzed using a log-rank test (Mantel-Cox) where **** = $p < 0.0001$.

Figure S3: Analysis of organ calcification. Flash frozen brain and formalin-fixed paraffin embedded heart were collected from 6-week-old mice. **(A)** Heart samples were stained with Alizarin Red and calcium depositions were manually counted and shown as Alizarin Red foci per animal (n = 3, 5, 5, 10 for WT, *Adar*$^{+/-}$, *RdRp*$^{tg/}$, *RdRp*$^{tg/-}$ *Adar*$^{+/-}$, respectively). Representative heart section images are shown to the right: (i) positive control heart provided by UCDSOM Research Histology Core Laboratory; (ii) RdRp$^{tg/-}$ Adar$^{+/-}$ heart without Alizarin red foci; (iii) RdRp$^{tg/-}$ Adar$^{+/-}$ heart with a positive focus. **(B)** Calcium was quantified from brain tissues (n = 3, 4, 5, 5). Data were analyzed using a one-way ANOVA followed by a Tukey tests; there were no significant differences between the groups. ns: not significant.

Figure S4: Predicted upstream regulators. Predicted upstream signaling regulators as determined by IPA in various genotype comparisons between WT, *Adar*$^{+/-}$, *RdRp*$^{tg/-}$, and *Adar*$^{+/-}$ *RdRp*$^{tg/-}$ mice where red/green indicates whether the gene itself is upregulated/downregulated in the RNA-seq and orange/blue indicates predicated activation/inhibition of the molecular pathway it regulates.

Figure S5: Loss of MDA5 rescues runting phenotype and abolished ISG upregulation. 6-week-old animals were weighed **(A)** and RNA was isolated from whole-brains for qPCR analysis of the ISGs Ifit1 **(B)**, Isg15 **(C)**, and Oasl2 **(D)**. Data were analyzed using a one-way ANOVA

followed by a Tukey tests where * = $p < 0.05$, ** = $p < 0.01$, *** = $p < 0.001$, **** = $p < 0.0001$. For (A), n = 4, 5, 6, 10, and 4 for WT, *Adar*$^{+/-}$, *RdRp*$^{tg/}$, *RdRp*$^{tg/-}$ *Adar*$^{+/-}$, and *RdRp*$^{tg/-}$ *Adar*$^{+/-}$ *Ifih1*$^{-/-}$, respectively. For (B-D), n = 4, 3, 5, 5, and 4. Data points represent individual animals with the mean for each group shown as a bar.

Figure S6: Disease and Biological Functions. Enriched diseases and biological functions across comparisons of gene expression changed between WT, *Adar*$^{+/-}$, *RdRp*$^{tg/-}$, and *Adar*$^{+/-}$ *RdRp*$^{tg/-}$ mice. Orange indicated that the disease or biological function is predicted to be enriched for and blue indicated is predicted to be inhibited.

Figure S7: Certain immune cell populations are unchanged in *RdRp*$^{tg/-}$ *Adar*$^{+/-}$ mice. Splenocytes from 4-5 week old mice were harvested and single cell, RBC-lsysed solutions were made for FACS analysis. **(A)** T cells, B cells, DCs, granulocytes, and NK cells show no difference across groups measured. n = 7, 7, 4, and 4 for WT, *Adar*$^{+/-}$, *RdRp*$^{tg/}$, and *RdRp*$^{tg/-}$ *Adar*$^{+/-}$, respectively. **(B)** DC subsets including pDCs, cDC1s, cDC2s, and moDCs show minor or no difference in populations across groups. n = 12, 7, 10, and 8 for WT, *Adar*$^{+/-}$, *RdRp*$^{tg/}$, and *RdRp*$^{tg/-}$ *Adar*$^{+/-}$, respectively. All data was analyzed using a one-way ANOVA followed by a Tukey test to determine significance. * = $p < 0.05$. Data represent individual animals, graphs show means and s.d.

Figure S8: Diseases and Biological Functions enriched for in A-to-I edited genes. Genes with A-to-I edit sites and RNA-seq-derived expression changes were analyzed using IPA to determine enriched diseases and biological functions across genotype comparisons (WT, *Adar*$^{+/-}$, *RdRp*$^{tg/-}$, and *Adar*$^{+/-}$ *RdRp*$^{tg/-}$). Orange indicates that the disease or biological function is predicted to be enriched for or activated and blue indicates is predicted to be inhibited.

Figure S9: Proportion of edited sites in ISG RNAs as a fraction of all uniquely edited sites per animal. Sites of A-to-I editing that were within an ISG were identified and the proportion of ISG edited sites out of all unique edited sites per animal was calculated. Bars indicate group means, dots represent individual animals, and the error bars are s.d. Data were analyzed using a one-way ANOVA followed by a Tukey tests where * = $p < 0.05$, *** = $p < 0.001$, **** = $p < 0.0001$, ns = not significant.

Figure S10: Flow cytometry gating strategy demonstrating live/dead cell gates and general gating strategy for B-cells, T-cells, granulocytes, neutrophils, and IFN upregulation of BST-2.

Figure S11: Flow cytometry gating strategy specific for plasma cells, germinal center B-cells, and T-cell subtypes.

Figure S12: Flow cytometry gating strategy specific for dendritic cell subtypes identification, activation and IFN upregulation.

Figure S13: Flow cytometry gating strategy specific for regulatory T-cells and Treg subtypes.

References

1. Rehwinkel, J., and Gack, M.U. (2020). RIG-I-like receptors: their regulation and roles in RNA sensing. Nature reviews. Immunology *20*, 537-551. 10.1038/s41577-020-0288-3.
2. Hornung, V., Ellegast, J., Kim, S., Brzozka, K., Jung, A., Kato, H., Poeck, H., Akira, S., Conzelmann, K.K., Schlee, M., et al. (2006). 5'-Triphosphate RNA is the ligand for RIG-I. Science *314*, 994-997. 10.1126/science.1132505.
3. Kato, H., Takeuchi, O., Mikamo-Satoh, E., Hirai, R., Kawai, T., Matsushita, K., Hiiragi, A., Dermody, T.S., Fujita, T., and Akira, S. (2008). Length-dependent recognition of double-stranded ribonucleic acids by retinoic acid-inducible gene-I and melanoma differentiation-associated gene 5. The Journal of experimental medicine *205*, 1601-1610. 10.1084/jem.20080091.
4. del Toro Duany, Y., Wu, B., and Hur, S. (2015). MDA5-filament, dynamics and disease. Curr Opin Virol *12*, 20-25. 10.1016/j.coviro.2015.01.011.
5. Dias Junior, A.G., Sampaio, N.G., and Rehwinkel, J. (2019). A Balancing Act: MDA5 in Antiviral Immunity and Autoinflammation. Trends Microbiol *27*, 75-85. 10.1016/j.tim.2018.08.007.
6. Kato, H., Takeuchi, O., Sato, S., Yoneyama, M., Yamamoto, M., Matsui, K., Uematsu, S., Jung, A., Kawai, T., Ishii, K.J., et al. (2006). Differential roles of MDA5 and RIG-I helicases in the recognition of RNA viruses. Nature *441*, 101-105. 10.1038/nature04734.
7. Gitlin, L., Barchet, W., Gilfillan, S., Cella, M., Beutler, B., Flavell, R.A., Diamond, M.S., and Colonna, M. (2006). Essential role of mda-5 in type I IFN responses to polyriboinosinic:polyribocytidylic acid and encephalomyocarditis picornavirus. Proceedings of the National Academy of Sciences of the United States of America *103*, 8459-8464. 10.1073/pnas.0603082103.
8. Feng, Q., Hato, S.V., Langereis, M.A., Zoll, J., Virgen-Slane, R., Peisley, A., Hur, S., Semler, B.L., van Rij, R.P., and van Kuppeveld, F.J. (2012). MDA5 detects the double-stranded RNA replicative form in picornavirus-infected cells. Cell reports *2*, 1187-1196. 10.1016/j.celrep.2012.10.005.
9. Ahmad, S., Mu, X., Yang, F., Greenwald, E., Park, J.W., Jacob, E., Zhang, C.Z., and Hur, S. (2018). Breaching Self-Tolerance to Alu Duplex RNA Underlies MDA5-Mediated Inflammation. Cell *172*, 797-810 e713. 10.1016/j.cell.2017.12.016.
10. Chung, H., Calis, J.J.A., Wu, X., Sun, T., Yu, Y., Sarbanes, S.L., Dao Thi, V.L., Shilvock, A.R., Hoffmann, H.H., Rosenberg, B.R., and Rice, C.M. (2018). Human ADAR1 Prevents Endogenous RNA from Triggering Translational Shutdown. Cell *172*, 811-824 e814. 10.1016/j.cell.2017.12.038.
11. Crow, Y.J., and Manel, N. (2015). Aicardi-Goutieres syndrome and the type I interferonopathies. Nature reviews. Immunology *15*, 429-440. 10.1038/nri3850.
12. Crow, Y.J., and Stetson, D.B. (2021). The type I interferonopathies: 10 years on. Nature reviews. Immunology. 10.1038/s41577-021-00633-9.
13. Hartner, J.C., Walkley, C.R., Lu, J., and Orkin, S.H. (2009). ADAR1 is essential for the maintenance of hematopoiesis and suppression of interferon signaling. Nature immunology *10*, 109-115. 10.1038/ni.1680.
14. Rice, G.I., Kasher, P.R., Forte, G.M., Mannion, N.M., Greenwood, S.M., Szynkiewicz, M., Dickerson, J.E., Bhaskar, S.S., Zampini, M., Briggs, T.A., et al. (2012). Mutations in ADAR1 cause Aicardi-Goutieres syndrome associated with a type I interferon signature. Nature genetics *44*, 1243-1248. 10.1038/ng.2414.
15. Mannion, N.M., Greenwood, S.M., Young, R., Cox, S., Brindle, J., Read, D., Nellaker, C., Vesely, C., Ponting, C.P., McLaughlin, P.J., et al. (2014). The RNA-editing enzyme ADAR1 controls innate immune responses to RNA. Cell reports *9*, 1482-1494. 10.1016/j.celrep.2014.10.041.

16. Samuel, C.E. (2019). Adenosine deaminase acting on RNA (ADAR1), a suppressor of double-stranded RNA-triggered innate immune responses. The Journal of biological chemistry *294*, 1710-1720. 10.1074/jbc.TM118.004166.
17. Song, B., Shiromoto, Y., Minakuchi, M., and Nishikura, K. (2022). The role of RNA editing enzyme ADAR1 in human disease. Wiley Interdiscip Rev RNA *13*, e1665. 10.1002/wrna.1665.
18. Liddicoat, B.J., Piskol, R., Chalk, A.M., Ramaswami, G., Higuchi, M., Hartner, J.C., Li, J.B., Seeburg, P.H., and Walkley, C.R. (2015). RNA editing by ADAR1 prevents MDA5 sensing of endogenous dsRNA as nonself. Science *349*, 1115-1120. 10.1126/science.aac7049.
19. George, C.X., Ramaswami, G., Li, J.B., and Samuel, C.E. (2016). Editing of Cellular Self-RNAs by Adenosine Deaminase ADAR1 Suppresses Innate Immune Stress Responses. The Journal of biological chemistry *291*, 6158-6168. 10.1074/jbc.M115.709014.
20. Hartner, J.C., Schmittwolf, C., Kispert, A., Muller, A.M., Higuchi, M., and Seeburg, P.H. (2004). Liver disintegration in the mouse embryo caused by deficiency in the RNA-editing enzyme ADAR1. The Journal of biological chemistry *279*, 4894-4902. 10.1074/jbc.M311347200.
21. Higuchi, M., Maas, S., Single, F.N., Hartner, J., Rozov, A., Burnashev, N., Feldmeyer, D., Sprengel, R., and Seeburg, P.H. (2000). Point mutation in an AMPA receptor gene rescues lethality in mice deficient in the RNA-editing enzyme ADAR2. Nature *406*, 78-81. 10.1038/35017558.
22. Tan, M.H., Li, Q., Shanmugam, R., Piskol, R., Kohler, J., Young, A.N., Liu, K.I., Zhang, R., Ramaswami, G., Ariyoshi, K., et al. (2017). Dynamic landscape and regulation of RNA editing in mammals. Nature *550*, 249-254. 10.1038/nature24041.
23. Crowl, J.T., Gray, E.E., Pestal, K., Volkman, H.E., and Stetson, D.B. (2017). Intracellular Nucleic Acid Detection in Autoimmunity. Annual review of immunology *35*, 313-336. 10.1146/annurev-immunol-051116-052331.
24. Heraud-Farlow, J.E., and Walkley, C.R. (2020). What do editors do? Understanding the physiological functions of A-to-I RNA editing by adenosine deaminase acting on RNAs. Open Biol *10*, 200085. 10.1098/rsob.200085.
25. Nakahama, T., and Kawahara, Y. (2023). The RNA-editing enzyme ADAR1: a regulatory hub that tunes multiple dsRNA-sensing pathways. Int Immunol *35*, 123-133. 10.1093/intimm/dxac056.
26. Heraud-Farlow, J.E., Chalk, A.M., Linder, S.E., Li, Q., Taylor, S., White, J.M., Pang, L., Liddicoat, B.J., Gupte, A., Li, J.B., and Walkley, C.R. (2017). Protein recoding by ADAR1-mediated RNA editing is not essential for normal development and homeostasis. Genome Biol *18*, 166. 10.1186/s13059-017-1301-4.
27. Chalk, A.M., Taylor, S., Heraud-Farlow, J.E., and Walkley, C.R. (2019). The majority of A-to-I RNA editing is not required for mammalian homeostasis. Genome Biol *20*, 268. 10.1186/s13059-019-1873-2.
28. Stetson, D.B., Ko, J.S., Heidmann, T., and Medzhitov, R. (2008). Trex1 prevents cell-intrinsic initiation of autoimmunity. Cell *134*, 587-598. 10.1016/j.cell.2008.06.032.
29. Crow, Y.J., Leitch, A., Hayward, B.E., Garner, A., Parmar, R., Griffith, E., Ali, M., Semple, C., Aicardi, J., Babul-Hirji, R., et al. (2006). Mutations in genes encoding ribonuclease H2 subunits cause Aicardi-Goutieres syndrome and mimic congenital viral brain infection. Nature genetics *38*, 910-916. 10.1038/ng1842.
30. Crow, Y.J., Hayward, B.E., Parmar, R., Robins, P., Leitch, A., Ali, M., Black, D.N., van Bokhoven, H., Brunner, H.G., Hamel, B.C., et al. (2006). Mutations in the gene encoding the 3'-5' DNA exonuclease TREX1 cause Aicardi-Goutieres syndrome at the AGS1 locus. Nature genetics *38*, 917-920. 10.1038/ng1845.

31. Rice, G.I., Del Toro Duany, Y., Jenkinson, E.M., Forte, G.M., Anderson, B.H., Ariaudo, G., Bader-Meunier, B., Baildam, E.M., Battini, R., Beresford, M.W., et al. (2014). Gain-of-function mutations in IFIH1 cause a spectrum of human disease phenotypes associated with upregulated type I interferon signaling. Nature genetics *46*, 503-509. 10.1038/ng.2933.
32. Oda, H., Nakagawa, K., Abe, J., Awaya, T., Funabiki, M., Hijikata, A., Nishikomori, R., Funatsuka, M., Ohshima, Y., Sugawara, Y., et al. (2014). Aicardi-Goutieres syndrome is caused by IFIH1 mutations. American journal of human genetics *95*, 121-125. 10.1016/j.ajhg.2014.06.007.
33. Uggenti, C., Lepelley, A., Depp, M., Badrock, A.P., Rodero, M.P., El-Daher, M.T., Rice, G.I., Dhir, S., Wheeler, A.P., Dhir, A., et al. (2020). cGAS-mediated induction of type I interferon due to inborn errors of histone pre-mRNA processing. Nature genetics *52*, 1364-1372. 10.1038/s41588-020-00737-3.
34. Wang, Q., Khillan, J., Gadue, P., and Nishikura, K. (2000). Requirement of the RNA editing deaminase ADAR1 gene for embryonic erythropoiesis. Science *290*, 1765-1768. 10.1126/science.290.5497.1765.
35. Wang, Q., Miyakoda, M., Yang, W., Khillan, J., Stachura, D.L., Weiss, M.J., and Nishikura, K. (2004). Stress-induced apoptosis associated with null mutation of ADAR1 RNA editing deaminase gene. The Journal of biological chemistry *279*, 4952-4961. 10.1074/jbc.M310162200.
36. Funabiki, M., Kato, H., Miyachi, Y., Toki, H., Motegi, H., Inoue, M., Minowa, O., Yoshida, A., Deguchi, K., Sato, H., et al. (2014). Autoimmune Disorders Associated with Gain of Function of the Intracellular Sensor MDA5. Immunity *40*, 199-212. 10.1016/j.immuni.2013.12.014.
37. Painter, M.M., Morrison, J.H., Zoecklein, L.J., Rinkoski, T.A., Watzlawik, J.O., Papke, L.M., Warrington, A.E., Bieber, A.J., Matchett, W.E., Turkowski, K.L., et al. (2015). Antiviral Protection via RdRP-Mediated Stable Activation of Innate Immunity. PLoS pathogens *11*, e1005311. 10.1371/journal.ppat.1005311.
38. Miller, C.M., Barrett, B.S., Chen, J., Morrison, J.H., Radomile, C., Santiago, M.L., and Poeschla, E.M. (2020). Systemic Expression of a Viral RdRP Protects against Retrovirus Infection and Disease. Journal of virology *94*. 10.1128/JVI.00071-20.
39. Bankers, L., Miller, C., Liu, G., Thongkittidilok, C., Morrison, J., and Poeschla, E.M. (2020). Development of interferon-stimulated gene expression from embryogenesis through adulthood, with and without constitutive MDA5 pathway activation. J Immunol *204*, 2791-2807.
40. Kerkvliet, J., Papke, L., and Rodriguez, M. (2011). Antiviral effects of a transgenic RNA-dependent RNA polymerase. Journal of virology *85*, 621-625. 10.1128/JVI.01626-10.
41. Kerkvliet, J., Zoecklein, L., Papke, L., Denic, A., Bieber, A.J., Pease, L.R., David, C.S., and Rodriguez, M. (2009). Transgenic expression of the 3D polymerase inhibits Theiler's virus infection and demyelination. Journal of virology *83*, 12279-12289. 10.1128/JVI.00664-09.
42. Crampton, S.P., Deane, J.A., Feigenbaum, L., and Bolland, S. (2012). Ifih1 gene dose effect reveals MDA5-mediated chronic type I IFN gene signature, viral resistance, and accelerated autoimmunity. J Immunol *188*, 1451-1459. 10.4049/jimmunol.1102705.
43. Gorman, J.A., Hundhausen, C., Errett, J.S., Stone, A.E., Allenspach, E.J., Ge, Y., Arkatkar, T., Clough, C., Dai, X., Khim, S., et al. (2017). The A946T variant of the RNA sensor IFIH1 mediates an interferon program that limits viral infection but increases the risk for autoimmunity. Nature immunology *18*, 744-752. 10.1038/ni.3766.
44. Morris, S.C., Cohen, P.L., and Eisenberg, R.A. (1990). Experimental induction of systemic lupus erythematosus by recognition of foreign Ia. Clin Immunol Immunopathol *57*, 263-273. 10.1016/0090-1229(90)90040-w.

45. Klarquist, J., and Janssen, E.M. (2015). The bm12 Inducible Model of Systemic Lupus Erythematosus (SLE) in C57BL/6 Mice. J Vis Exp, e53319. 10.3791/53319.
46. Stebegg, M., Kumar, S.D., Silva-Cayetano, A., Fonseca, V.R., Linterman, M.A., and Graca, L. (2018). Regulation of the Germinal Center Response. Front Immunol *9*, 2469. 10.3389/fimmu.2018.02469.
47. Tsokos, G.C., Lo, M.S., Costa Reis, P., and Sullivan, K.E. (2016). New insights into the immunopathogenesis of systemic lupus erythematosus. Nat Rev Rheumatol *12*, 716-730. 10.1038/nrrheum.2016.186.
48. Zhuang, H., Szeto, C., Han, S., Yang, L., and Reeves, W.H. (2015). Animal Models of Interferon Signature Positive Lupus. Front Immunol *6*, 291. 10.3389/fimmu.2015.00291.
49. Dominguez-Villar, M., and Hafler, D.A. (2018). Regulatory T cells in autoimmune disease. Nature immunology *19*, 665-673. 10.1038/s41590-018-0120-4.
50. Kim, J., Lahl, K., Hori, S., Loddenkemper, C., Chaudhry, A., deRoos, P., Rudensky, A., and Sparwasser, T. (2009). Cutting edge: depletion of Foxp3+ cells leads to induction of autoimmunity by specific ablation of regulatory T cells in genetically targeted mice. J Immunol *183*, 7631-7634. 10.4049/jimmunol.0804308.
51. Sun, T., Yu, Y., Wu, X., Acevedo, A., Luo, J.D., Wang, J., Schneider, W.M., Hurwitz, B., Rosenberg, B.R., Chung, H., and Rice, C.M. (2021). Decoupling expression and editing preferences of ADAR1 p150 and p110 isoforms. Proceedings of the National Academy of Sciences of the United States of America *118*. 10.1073/pnas.2021757118.
52. George, C.X., and Samuel, C.E. (1999). Human RNA-specific adenosine deaminase ADAR1 transcripts possess alternative exon 1 structures that initiate from different promoters, one constitutively active and the other interferon inducible. Proceedings of the National Academy of Sciences of the United States of America *96*, 4621-4626. 10.1073/pnas.96.8.4621.
53. Yang, J.H., Nie, Y., Zhao, Q., Su, Y., Pypaert, M., Su, H., and Rabinovici, R. (2003). Intracellular localization of differentially regulated RNA-specific adenosine deaminase isoforms in inflammation. The Journal of biological chemistry *278*, 45833-45842. 10.1074/jbc.M308612200.
54. Singleton, E.B., and Merten, D.F. (1973). An unusual syndrome of widened medullary cavities of the metacarpals and phalanges, aortic calcification and abnormal dentition. Pediatr Radiol *1*, 2-7. 10.1007/BF00972817.
55. Feigenbaum, A., Muller, C., Yale, C., Kleinheinz, J., Jezewski, P., Kehl, H.G., MacDougall, M., Rutsch, F., and Hennekam, R.C. (2013). Singleton-Merten syndrome: an autosomal dominant disorder with variable expression. American journal of medical genetics. Part A *161A*, 360-370. 10.1002/ajmg.a.35732.
56. Rutsch, F., MacDougall, M., Lu, C., Buers, I., Mamaeva, O., Nitschke, Y., Rice, G.I., Erlandsen, H., Kehl, H.G., Thiele, H., et al. (2015). A specific IFIH1 gain-of-function mutation causes Singleton-Merten syndrome. American journal of human genetics *96*, 275-282. 10.1016/j.ajhg.2014.12.014.
57. Pettersson, M., Bergendal, B., Norderyd, J., Nilsson, D., Anderlid, B.M., Nordgren, A., and Lindstrand, A. (2017). Further evidence for specific IFIH1 mutation as a cause of Singleton-Merten syndrome with phenotypic heterogeneity. American journal of medical genetics. Part A *173*, 1396-1399. 10.1002/ajmg.a.38214.
58. Bursztejn, A.C., Briggs, T.A., del Toro Duany, Y., Anderson, B.H., O'Sullivan, J., Williams, S.G., Bodemer, C., Fraitag, S., Gebhard, F., Leheup, B., et al. (2015). Unusual cutaneous features associated with a heterozygous gain-of-function mutation in IFIH1: overlap between Aicardi-Goutieres and Singleton-Merten syndromes. The British journal of dermatology *173*, 1505-1513. 10.1111/bjd.14073.
59. Buers, I., Rice, G.I., Crow, Y.J., and Rutsch, F. (2017). MDA5-Associated Neuroinflammation and the Singleton-Merten Syndrome: Two Faces of the Same Type I

Interferonopathy Spectrum. J Interferon Cytokine Res *37*, 214-219. 10.1089/jir.2017.0004.

60. de Carvalho, L.M., Ngoumou, G., Park, J.W., Ehmke, N., Deigendesch, N., Kitabayashi, N., Melki, I., Souza, F.F.L., Tzschach, A., Nogueira-Barbosa, M.H., et al. (2017). Musculoskeletal Disease in MDA5-Related Type I Interferonopathy: A Mendelian Mimic of Jaccoud's Arthropathy. Arthritis Rheumatol *69*, 2081-2091. 10.1002/art.40179.
61. Xiao, W., Feng, J., Long, H., Xiao, B., and Luo, Z.H. (2021). Case Report: Aicardi-Goutieres Syndrome and Singleton-Merten Syndrome Caused by a Gain-of-Function Mutation in IFIH1. Front Genet *12*, 660953. 10.3389/fgene.2021.660953.
62. Jang, M.A., Kim, E.K., Now, H., Nguyen, N.T., Kim, W.J., Yoo, J.Y., Lee, J., Jeong, Y.M., Kim, C.H., Kim, O.H., et al. (2015). Mutations in DDX58, which encodes RIG-I, cause atypical Singleton-Merten syndrome. American journal of human genetics *96*, 266-274. 10.1016/j.ajhg.2014.11.019.
63. Maelfait, J., and Rehwinkel, J. (2023). The Z-nucleic acid sensor ZBP1 in health and disease. The Journal of experimental medicine *220*. 10.1084/jem.20221156.
64. Neil, S.J., Zang, T., and Bieniasz, P.D. (2008). Tetherin inhibits retrovirus release and is antagonized by HIV-1 Vpu. Nature *451*, 425-430.
65. Liberatore, R.A., and Bieniasz, P.D. (2011). Tetherin is a key effector of the antiretroviral activity of type I interferon in vitro and in vivo. Proceedings of the National Academy of Sciences of the United States of America *108*, 18097-18101. 10.1073/pnas.1113694108.
66. Morrison, J.H., and Poeschla, E.M. (2023). The Feline Immunodeficiency Virus Envelope Signal Peptide Is a Tetherin Antagonizing Protein. mBio *14*, e0016123. 10.1128/mbio.00161-23.
67. Kassiotis, G., and Stoye, J.P. (2016). Immune responses to endogenous retroelements: taking the bad with the good. Nature reviews. Immunology *16*, 207-219. 10.1038/nri.2016.27.
68. Zhang, T., Yin, C., Fedorov, A., Qiao, L., Bao, H., Beknazarov, N., Wang, S., Gautam, A., Williams, R.M., Crawford, J.C., et al. (2022). ADAR1 masks the cancer immunotherapeutic promise of ZBP1-driven necroptosis. Nature *606*, 594-602. 10.1038/s41586-022-04753-7.
69. Theiler, M., and Smith, H.H. (1937). The Use of Yellow Fever Virus Modified by in Vitro Cultivation for Human Immunization. The Journal of experimental medicine *65*, 787-800. 10.1084/jem.65.6.787.
70. Theiler, M. (1937). Spontaneous Encephalomyelitis of Mice, a New Virus Disease. The Journal of experimental medicine *65*, 705-719.
71. Rehwinkel, J., and Mehdipour, P. (2024). ADAR1: from basic mechanisms to inhibitors. Trends Cell Biol. 10.1016/j.tcb.2024.06.006.
72. Maurano, M., Snyder, J.M., Connelly, C., Henao-Mejia, J., Sidrauski, C., and Stetson, D.B. (2021). Protein kinase R and the integrated stress response drive immunopathology caused by mutations in the RNA deaminase ADAR1. Immunity *54*, 1948-1960 e1945. 10.1016/j.immuni.2021.07.001.
73. Liang, Z., Chalk, A.M., Taylor, S., Goradia, A., Heraud-Farlow, J.E., and Walkley, C.R. (2023). The phenotype of the most common human ADAR1p150 Zalpha mutation P193A in mice is partially penetrant. EMBO Rep, e55835. 10.15252/embr.202255835.
74. Guo, X., Steinman, R.A., Sheng, Y., Cao, G., Wiley, C.A., and Wang, Q. (2022). An AGS-associated mutation in ADAR1 catalytic domain results in early-onset and MDA5-dependent encephalopathy with IFN pathway activation in the brain. J Neuroinflammation *19*, 285. 10.1186/s12974-022-02646-0.

75. Soda, N., Sakai, N., Kato, H., Takami, M., and Fujita, T. (2019). Singleton-Merten Syndrome-like Skeletal Abnormalities in Mice with Constitutively Activated MDA5. J Immunol *203*, 1356-1368. 10.4049/jimmunol.1900354.
76. Emralino, F.L., Satoh, S., Sakai, N., Takami, M., Takeuchi, F., Yan, N., Rutsch, F., Fujita, T., and Kato, H. (2022). Double-Stranded RNA Induces Mortality in an MDA5-Mediated Type I Interferonopathy Model. J Immunol *209*, 2093-2103. 10.4049/jimmunol.2200367.
77. Eisenberg, E., and Levanon, E.Y. (2018). A-to-I RNA editing - immune protector and transcriptome diversifier. Nature reviews. Genetics *19*, 473-490. 10.1038/s41576-018-0006-1.
78. Roth, S.H., Danan-Gotthold, M., Ben-Izhak, M., Rechavi, G., Cohen, C.J., Louzoun, Y., and Levanon, E.Y. (2018). Increased RNA Editing May Provide a Source for Autoantigens in Systemic Lupus Erythematosus. Cell reports *23*, 50-57. 10.1016/j.celrep.2018.03.036.
79. Maas, S., Kawahara, Y., Tamburro, K.M., and Nishikura, K. (2006). A-to-I RNA editing and human disease. RNA biology *3*, 1-9. 10.4161/rna.3.1.2495.
80. Bouxsein, M.L., Boyd, S.K., Christiansen, B.A., Guldberg, R.E., Jepsen, K.J., and Muller, R. (2010). Guidelines for assessment of bone microstructure in rodents using micro-computed tomography. J Bone Miner Res *25*, 1468-1486. 10.1002/jbmr.141.
81. Schriefer, J.L., Robling, A.G., Warden, S.J., Fournier, A.J., Mason, J.J., and Turner, C.H. (2005). A comparison of mechanical properties derived from multiple skeletal sites in mice. J Biomech *38*, 467-475. 10.1016/j.jbiomech.2004.04.020.
82. Heveran, C.M., Schurman, C.A., Acevedo, C., Livingston, E.W., Howe, D., Schaible, E.G., Hunt, H.B., Rauff, A., Donnelly, E., Carpenter, R.D., et al. (2019). Chronic kidney disease and aging differentially diminish bone material and microarchitecture in C57Bl/6 mice. Bone *127*, 91-103. 10.1016/j.bone.2019.04.019.
83. Barraza, R.A., McLaren, J.W., and Poeschla, E.M. (2010). Prostaglandin Pathway Gene Therapy for Sustained Reduction of Intraocular Pressure. Molecular Therapy *18*, 491-501. mt2009278 10.1038/mt.2009.278.

Figures 1-7

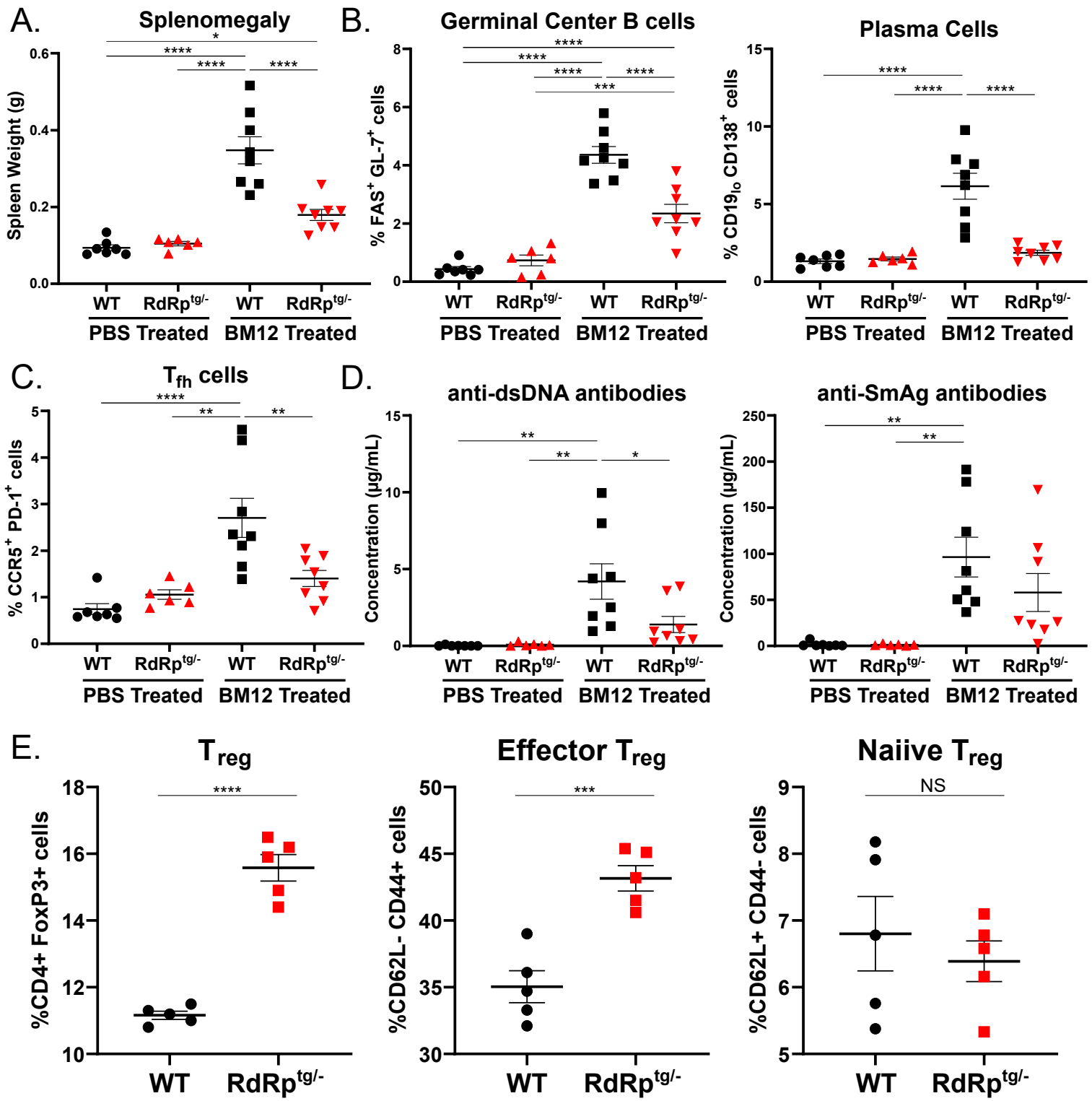

Figure 1

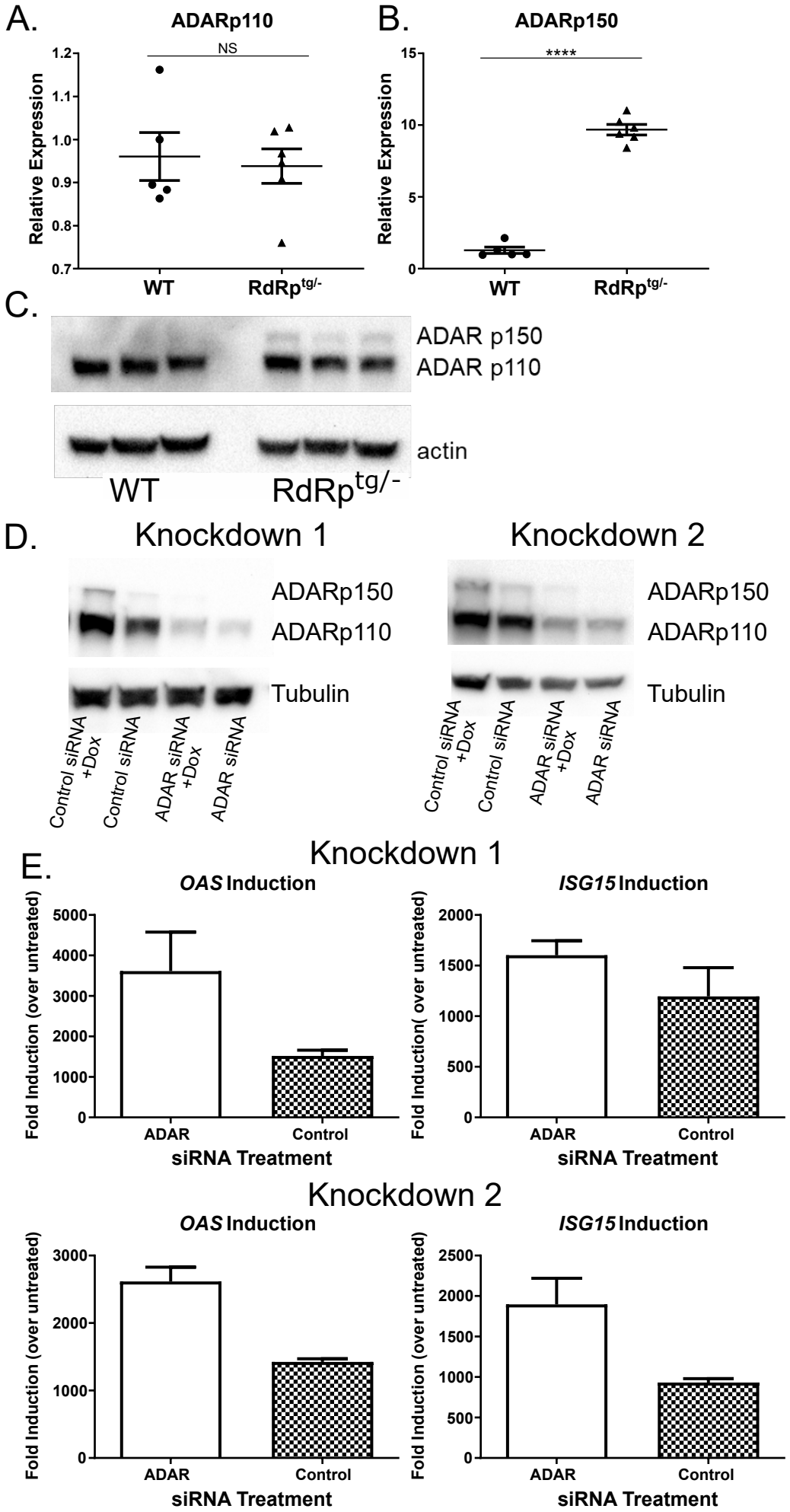
A.
ADARp110
NS
Relative Expression
1.2
1.1
1.0
0.9
0.8
0.7
WT
RdRp tg/-
B.
ADARp150
****
Relative Expression
15
10
5
0
WT
RdRp tg/-
C.
ADAR p150
ADAR p110
actin
WT
RdRp tg/-
D.
Knockdown 1
Knockdown 2
ADARp150
ADARp110
Tubulin
Control siRNA +Dox
Control siRNA
ADAR siRNA +Dox
ADAR siRNA
E.
Knockdown 1
OAS Induction
ISG15 Induction
Fold Induction (over untreated)
Fold Induction(over untreated)
5000
4000
3000
2000
1000
0
2000
1500
1000
500
ADAR
Control
siRNA Treatment
Knockdown 2
OAS Induction
ISG15 Induction
3000
2000
1000
0
2500
2000
1500
1000
500

Figure 2

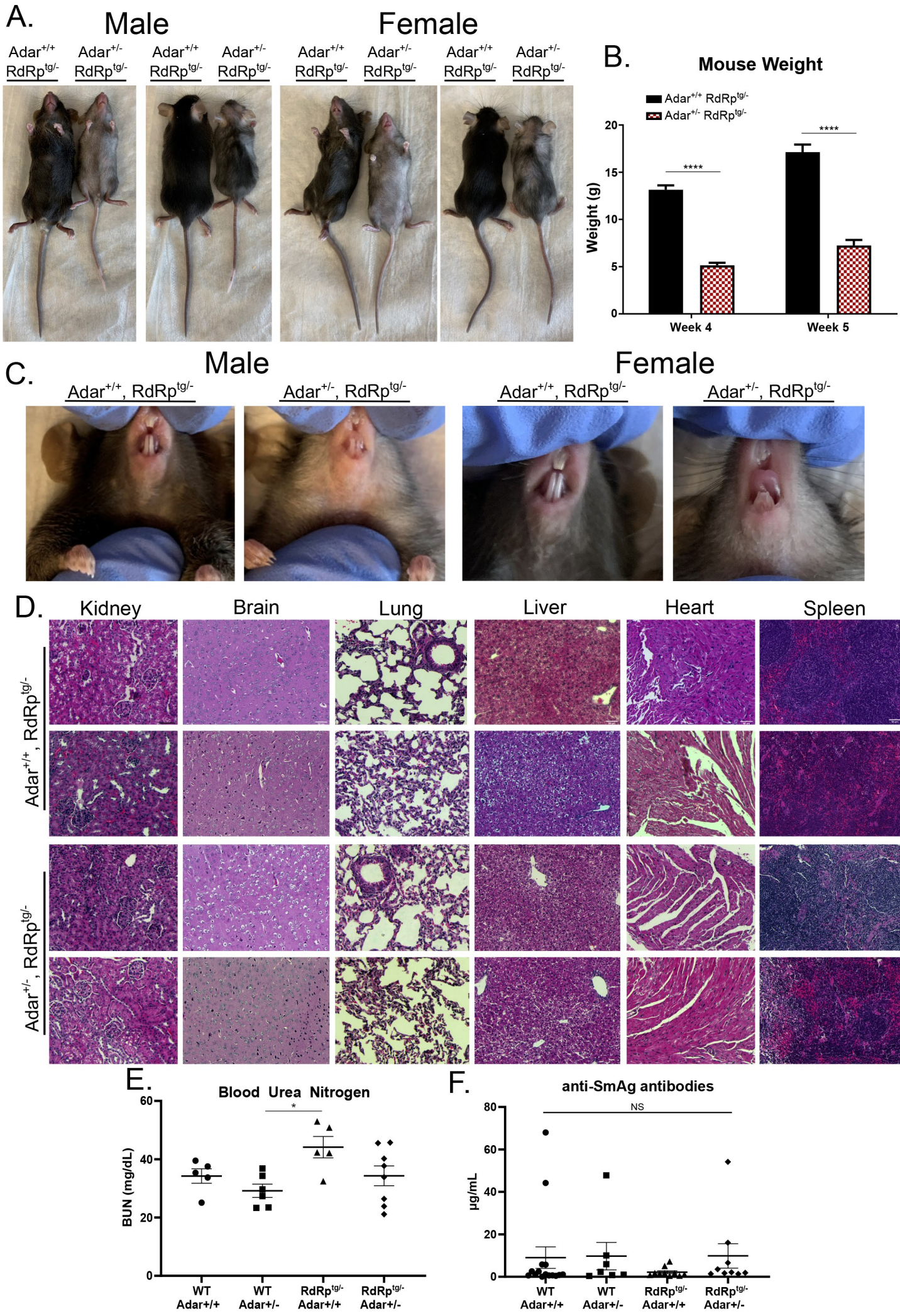
A.
Male
Female
Adar+/+ RdRptg/-
Adar+/- RdRptg/-
B.
Mouse Weight
Adar+/+ RdRptg/-
Adar+/- RdRptg/-
Weight (g)
****
Week 4
Week 5
C.
Male
Female
Adar+/+, RdRptg/-
Adar+/-, RdRptg/-
D.
Kidney
Brain
Lung
Liver
Heart
Spleen
Adar+/+, RdRptg/-
Adar+/-, RdRptg/-
E.
Blood Urea Nitrogen
BUN (mg/dL)
*
WT Adar+/+
WT Adar+/-
RdRptg/- Adar+/+
RdRptg/- Adar+/-
F.
anti-SmAg antibodies
µg/mL
NS

Figure 3

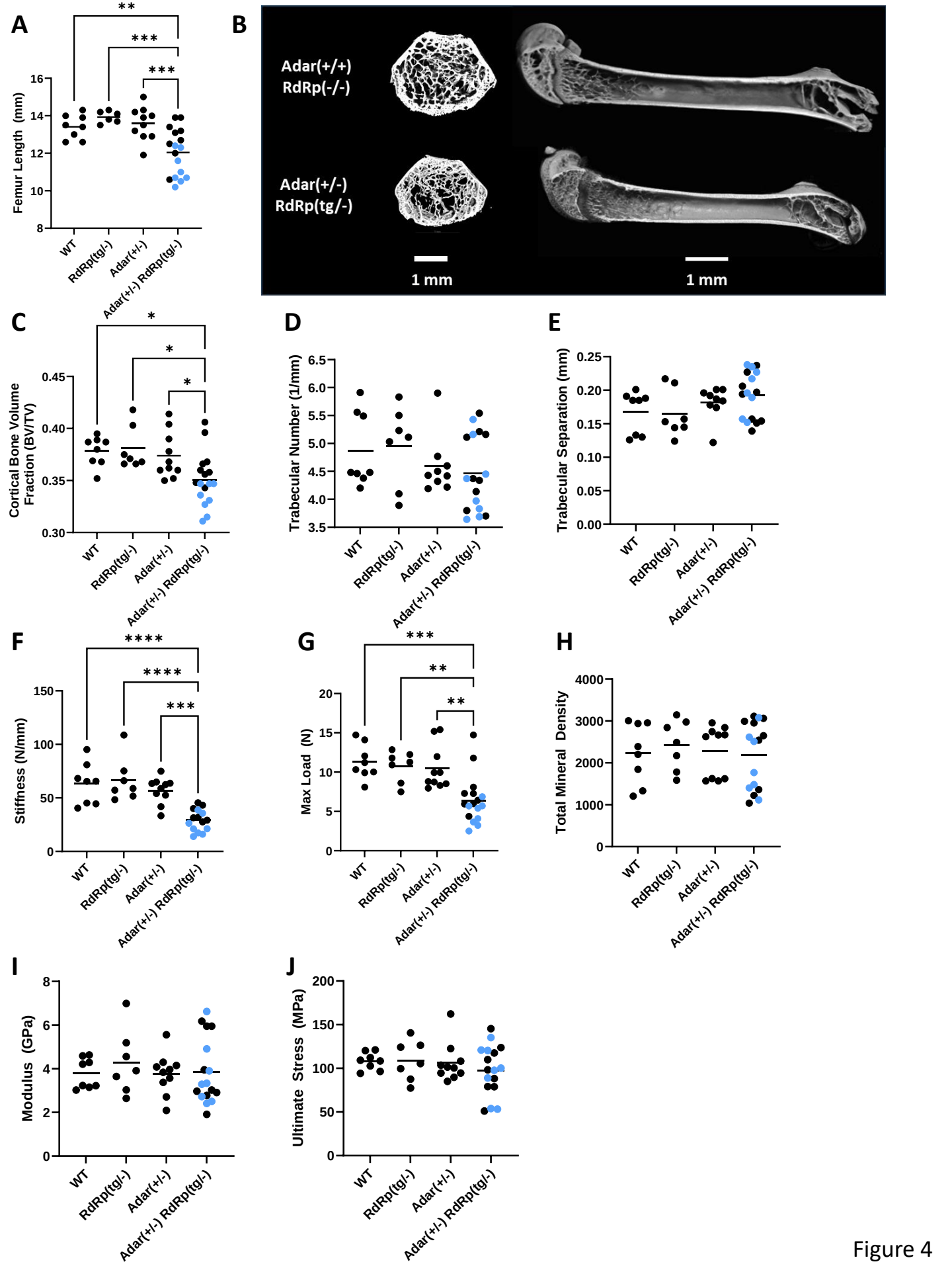
A
Femur Length (mm)
WT
RdRp(tg/-)
Adar(+/-)
Adar(+/-) RdRp(tg/-)
B
Adar(+/+)
RdRp(-/-)
Adar(+/-)
RdRp(tg/-)
1 mm
1 mm
C
Cortical Bone Volume Fraction (BV/TV)
D
Trabecular Number (1/mm)
E
Trabecular Separation (mm)
F
Stiffness (N/mm)
G
Max Load (N)
H
Total Mineral Density
I
Modulus (GPa)
J
Ultimate Stress (MPa)

Figure 4

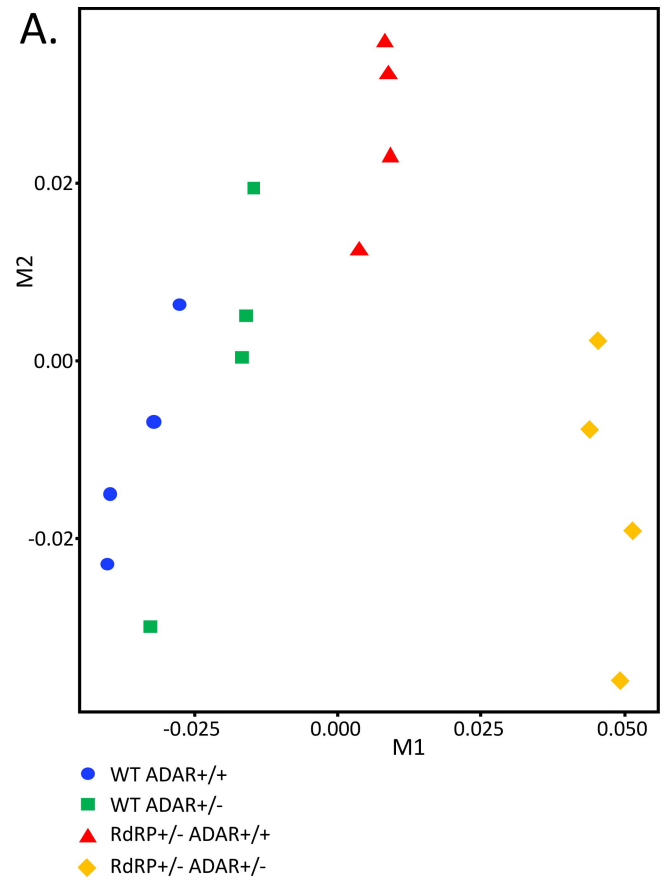

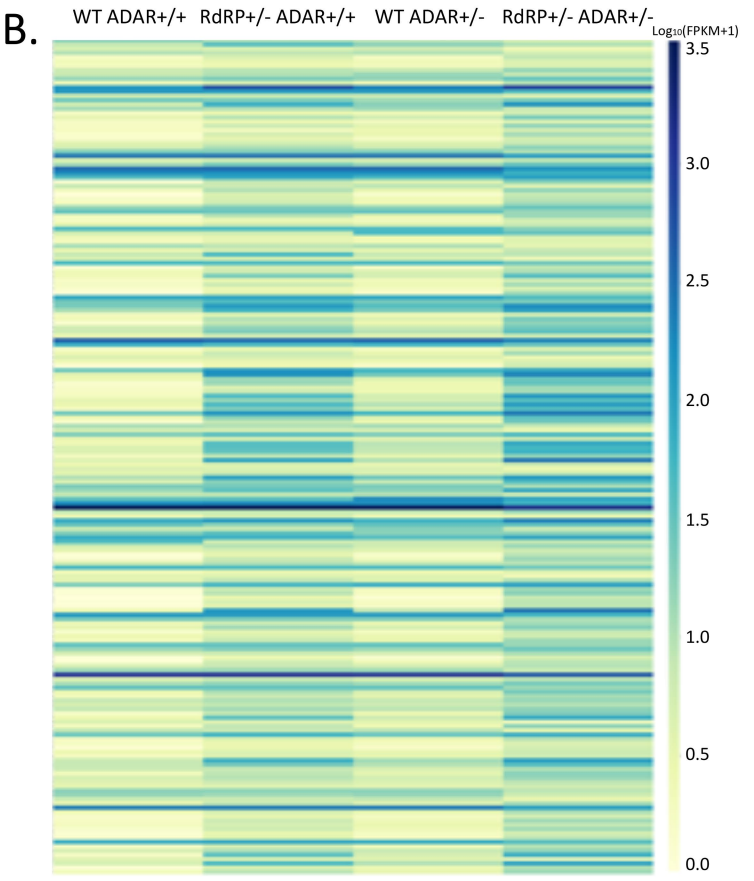

C.

Comparison	Up DEGs	Up ISGs (%)	Down DEGs	Down ISGs (%)	Total DEGs	Total ISGs (%)
WT ADAR+/+ vs. RdRP+/- ADAR+/+	96	84 (87.5%)	6	2 (33.3%)	102	86 (84.3%)
WT ADAR+/+ vs. WT ADAR+/-	30	27 (90.0%)	5	3 (60.0%)	35	30 (85.7%)
WT ADAR+/+ vs. RdRP+/- ADAR+/-	151	136 (90.1%)	75	38 (50.7%)	226	174 (76.9%)
RdRP+/- ADAR+/+ vs. WT ADAR+/-	6	4 (66.7%)	83	73 (87.9%)	89	77 (86.5%)
RdRP+/- ADAR+/+ vs. RdRP+/- ADAR+/-	64	59 (92.2%)	67	35 (52.2%)	131	94 (71.8%)
WT ADAR+/- vs. RdRP+/- ADAR+/-	137	124 (90.5%)	75	37 (49.3%)	212	161 (75.9%)

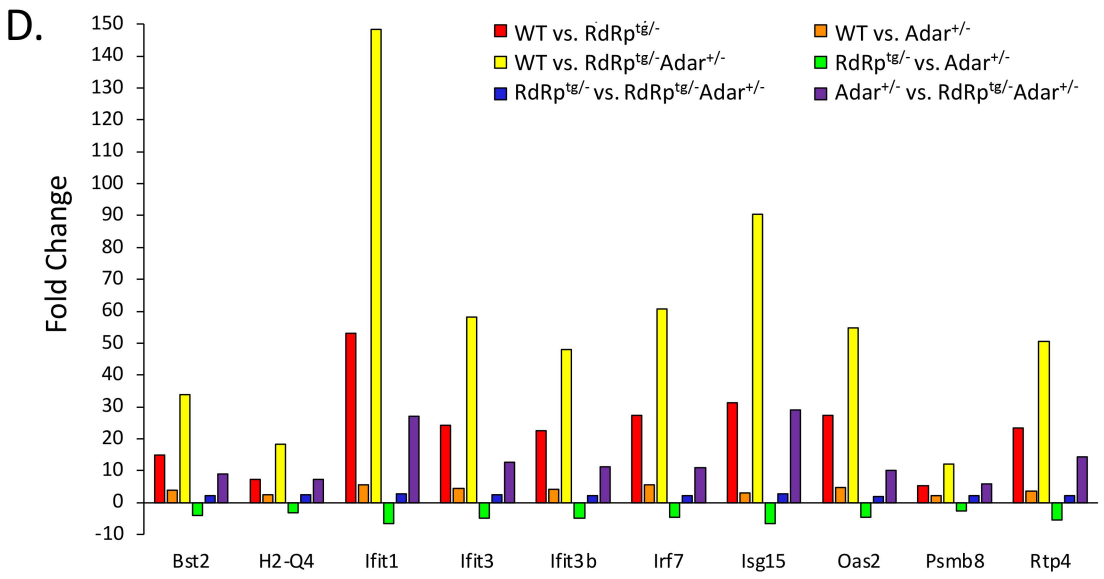

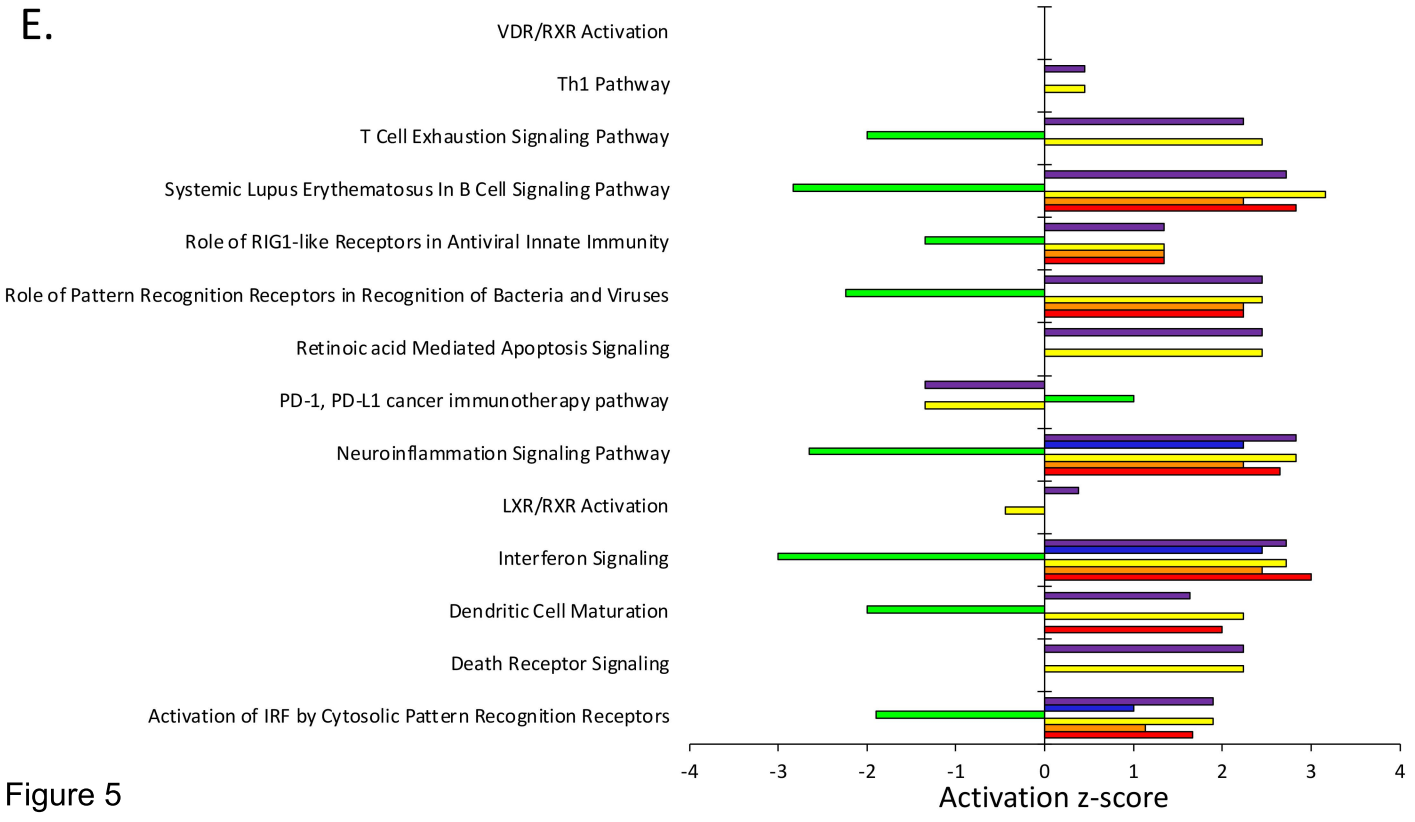

Figure 5

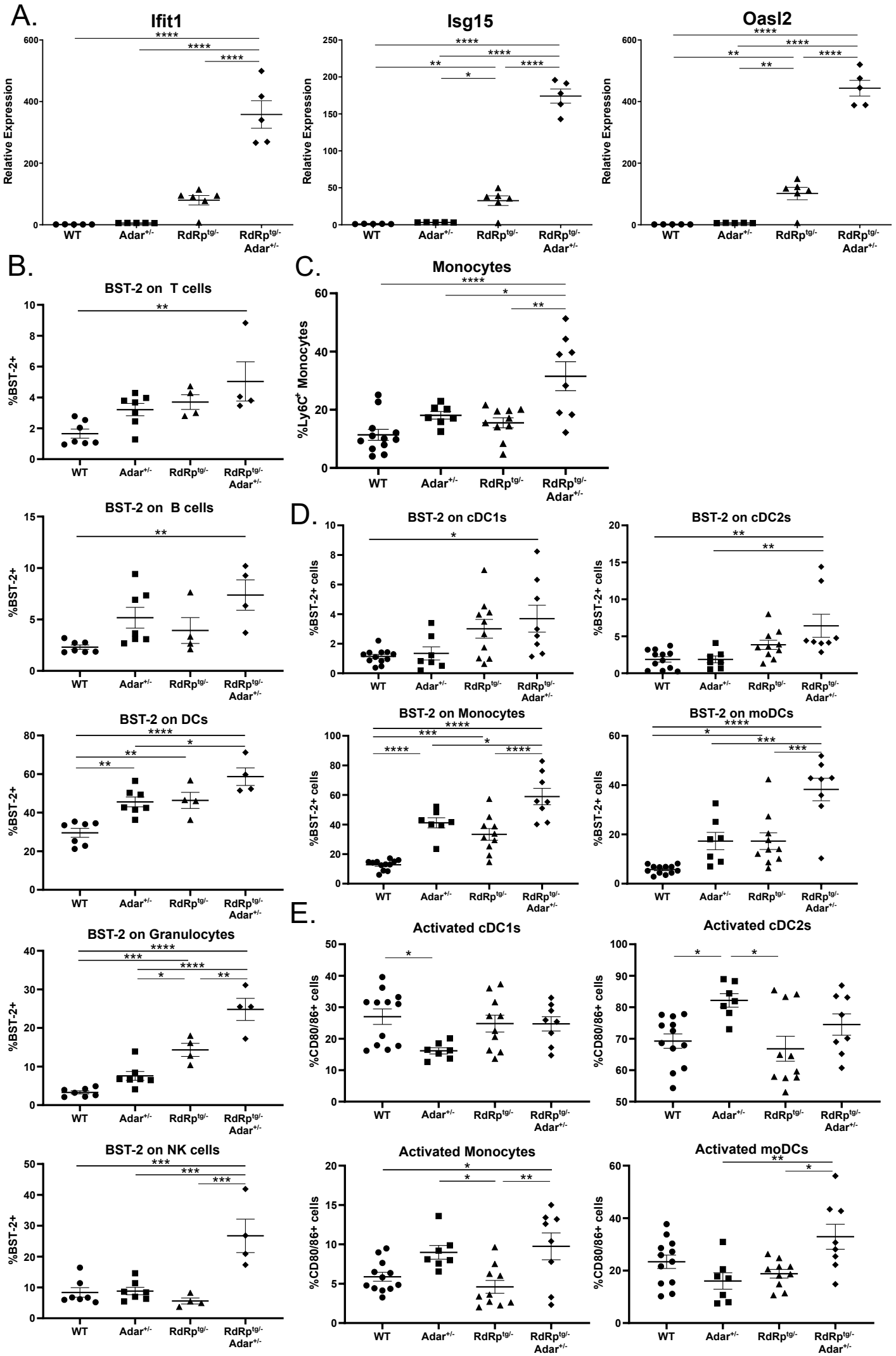
A.
Ifit1
Isg15
Oasl2
Relative Expression
WT
Adar+/-
RdRptg/-
RdRptg/- Adar+/-
B.
BST-2 on T cells
BST-2 on B cells
BST-2 on DCs
BST-2 on Granulocytes
BST-2 on NK cells
%BST-2+
C.
Monocytes
%Ly6C+ Monocytes
D.
BST-2 on cDC1s
BST-2 on cDC2s
BST-2 on Monocytes
BST-2 on moDCs
%BST-2+ cells
E.
Activated cDC1s
Activated cDC2s
Activated Monocytes
Activated moDCs
%CD80/86+ cells

Figure 6

A.

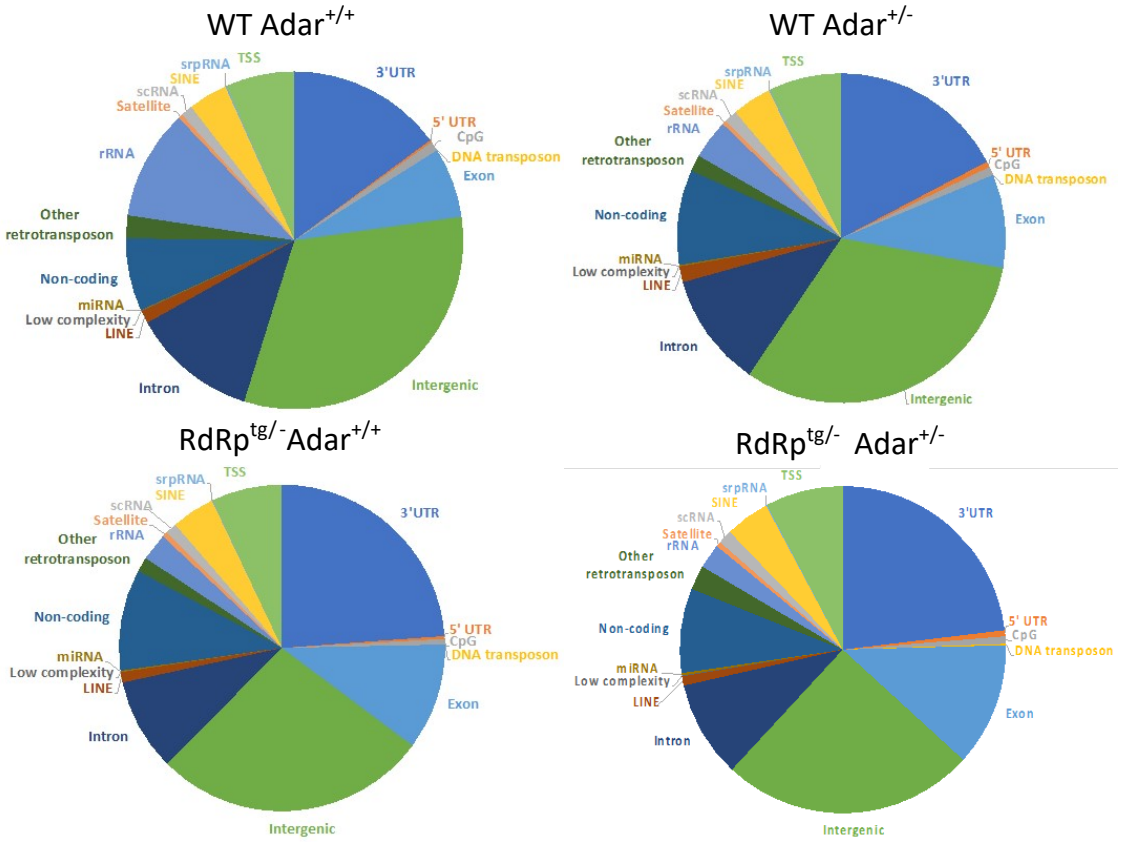

B.

	WT	RdRp$^{tg/-}$	Adar$^{+/-}$	RdRp$^{tg/-}$ Adar$^{+/-}$
Genes	2610	1989	2233	3077
Sites	1317	1446	1431	2174

Annotation	**WT**	**RdRp$^{tg/-}$**	**Adar$^{+/-}$**	**RdRp$^{tg/-}$ Adar$^{+/-}$**
3'UTR	210	344	247	500
5' UTR	3	4	8	13
CpG	13	8	12	16
DNA transposon	0	0	0	3
Exon	95	152	131	264
Intergenic	452	393	450	544
Intron	170	132	160	207
LINE	17	15	22	20
Low complexity	1	0	0	2
miRNA	1	2	2	5
Non-coding	98	145	133	181
Other retrotransposon	31	21	23	52
rRNA	149	39	55	53
Satellite	6	8	6	11
scRNA	16	16	18	30
SINE	53	62	55	95
srpRNA	2	1	2	2
TSS	93	101	102	167

C.

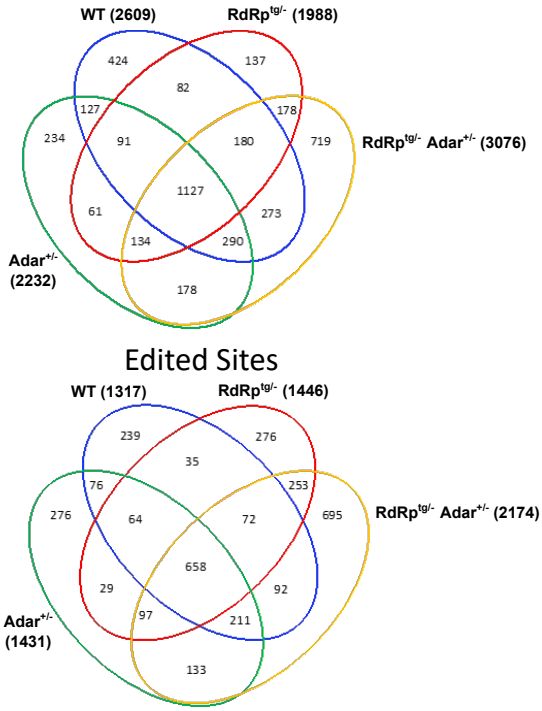

D.

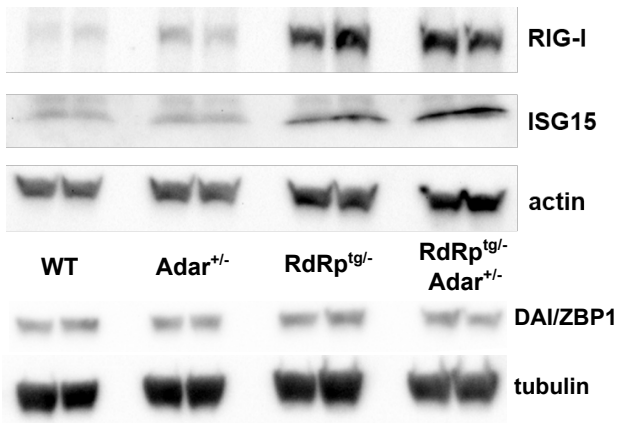

E.

RNAseq Expression Levels

	WT vs. Adar$^{+/-}$	WT vs. RdRp$^{tg/-}$	WT vs. RdRp$^{tg/-}$ Adar$^{+/-}$
RIG-I	ns	9.330	15.600
ISG15	3.099	31.218	90.325
ZBP1	2.919	4.013	5.471

F.

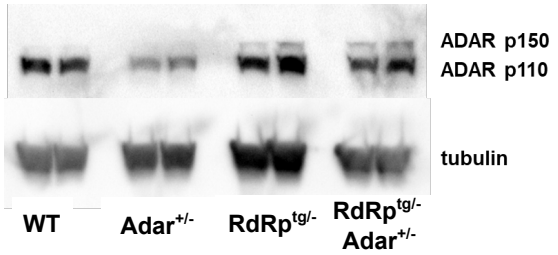

Figure 7

Figure S1 - S13

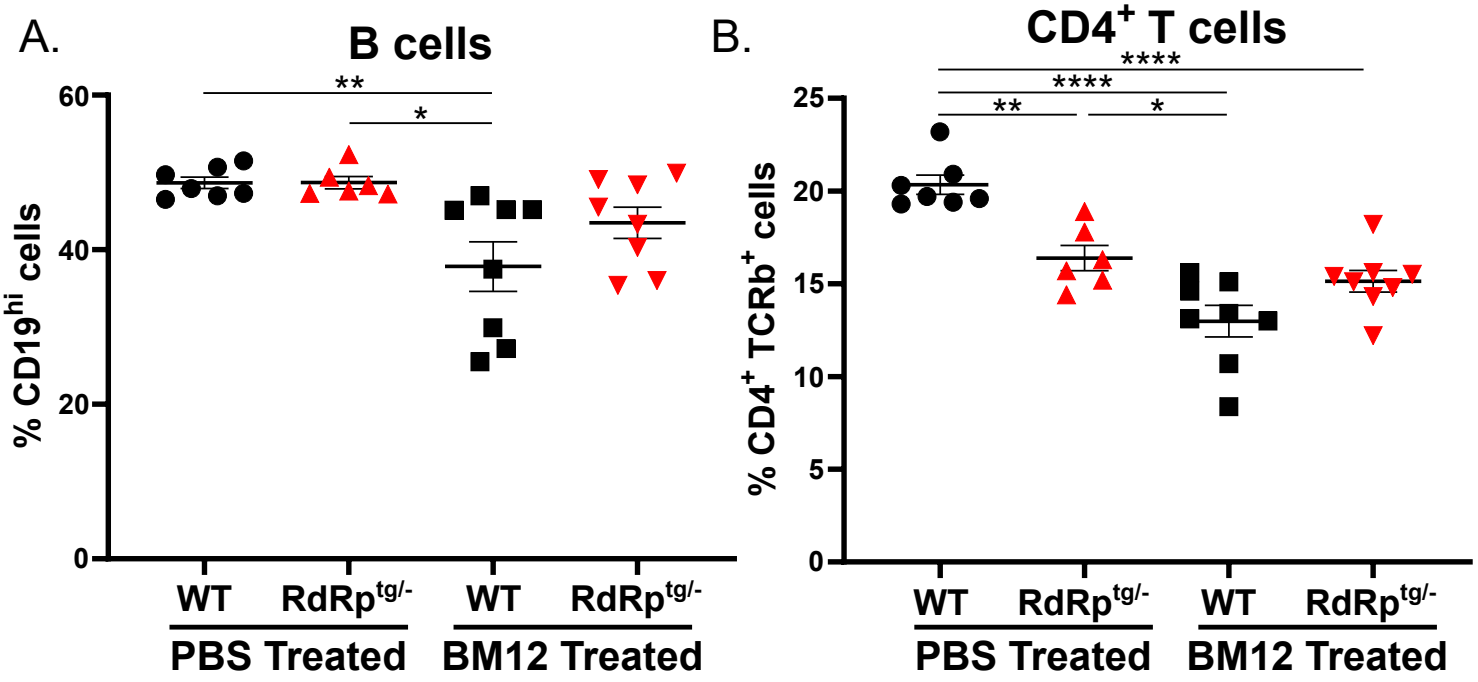

Supplemental Figure 1

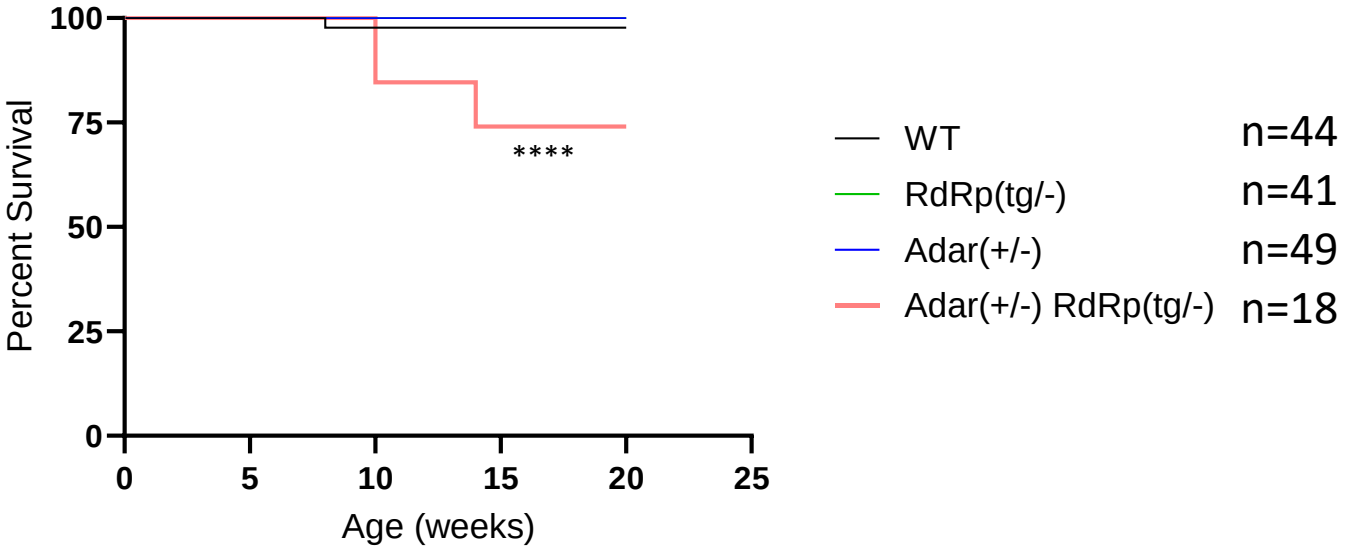

Supplemental Figure 2

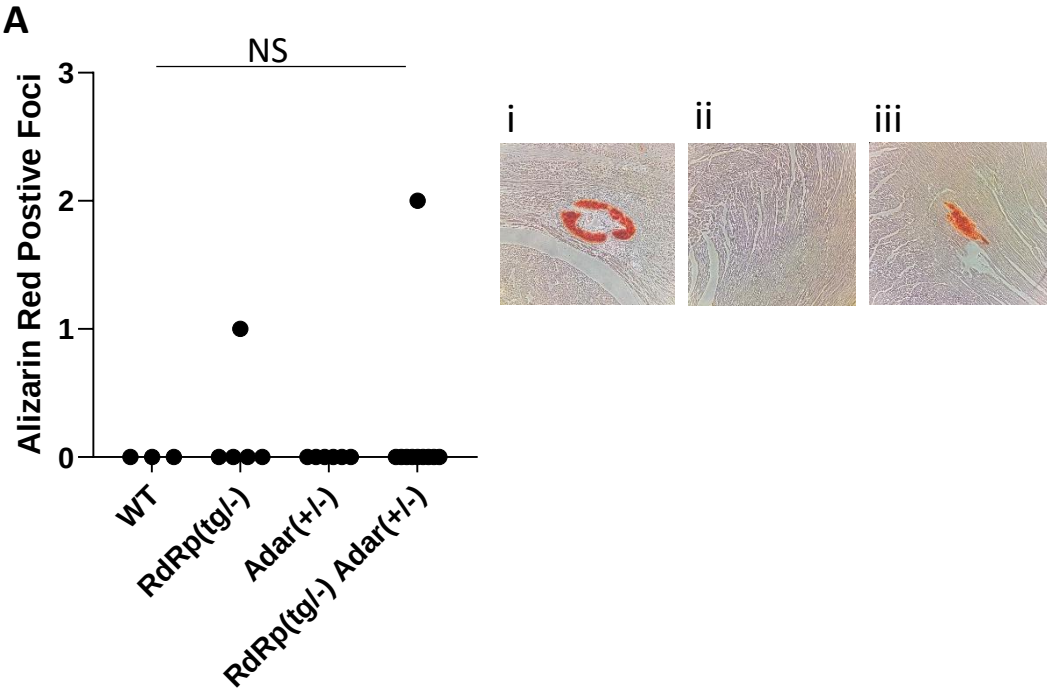

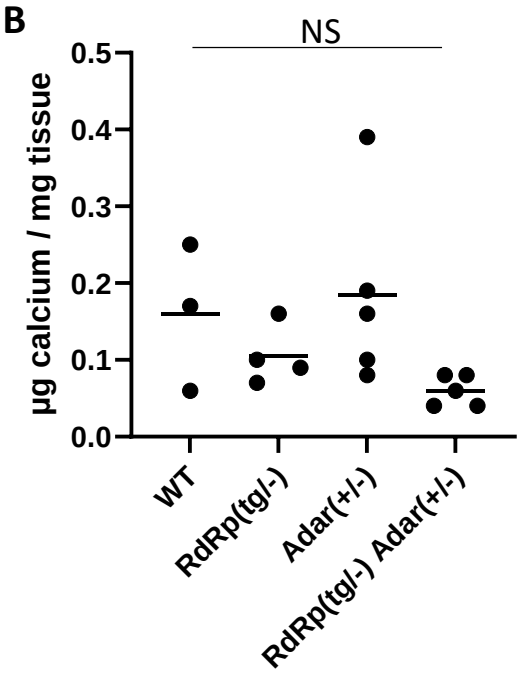

Supplemental Figure 3

	WT vs. RdRp$^{tg/-}$		WT vs. Adar$^{+/-}$		WT vs. RdRp$^{tg/-}$ Adar$^{+/-}$		RdRp$^{tg/-}$ vs. Adar$^{+/-}$		RdRp$^{tg/-}$ vs. RdRp$^{tg/-}$ Adar$^{+/-}$		Adar$^{+/-}$ vs. RdRp$^{tg/-}$ Adar$^{+/-}$	
Upstream Regulators	**Expr Log Ratio**	**Activation z-score**	**Expr Log Ratio**	**Activation z-score**	**Expr Log Ratio**	**Activation z-score**	**Expr Log Ratio**	**Activation z-score**	**Expr Log Ratio**	**Activation z-score**	**Expr Log Ratio**	**Activation z-score**
DDX58	3.222	3.645	1.092	2.988	3.963	4.241	-2.13	-3.78	0.742	3.497	2.872	4.241
EIF2AK2	3.038	3.556	1.055	2.611	3.751	3.952	-1.983	-3.414	0.713	NA	2.696	3.825
IFI16	NA	2.608	2.272	2.784	5.617	2.952	-1.743	-2.952	1.603	2.599	3.345	2.952
IFIH1	3.038	2.923	1.104	2.939	3.915	3.375	-1.934	-3.234	0.878	2.937	2.812	3.234
IL33	-0.237	NA	0.137	NA	-0.885	2.172	0.374	NA	-0.648	2.172	-1.022	2.172
IRF1	NA	4.776	0.445	4.059	1.503	5.423	-0.409	-4.8	0.648	3.542	1.058	5.423
IRF7	4.775	6.158	2.476	5.518	5.927	7.107	-2.299	-6.608	1.152	5.42	3.451	6.894
IRF9	3.408	2.603	1.046	1.944	3.878	1.897	-2.362	-2.603	0.47	1.966	2.832	1.897
Irgm1	3.167	-3.108	0.997	-3.413	4.208	-3.555	-2.17	3.555	1.041	-3.264	3.211	-3.555
PARP9	2.591	2.621	1.003	2.219	3.582	2.178	-1.588	-2.804	0.991	2.433	2.579	2.178
PML	0.878	3.582	0.193	3.44	1.323	3.597	-0.685	-3.843	0.445	3.138	1.13	3.467
PNPT1	0.562	-5.196	0.16	-4.772	1.181	-5.547	-0.403	5.174	0.619	-3.973	1.021	-5.547
SOCS1	NA	-4.28	0.316	-4.286	1.675	-5.01	-0.619	4.506	0.74	-4.171	1.359	-4.915
STAT1	3.57	5.727	0.956	5.108	4.218	6.643	-2.614	-6.128	0.648	5.063	3.262	6.643
STAT2	1.815	3.095	0.403	2.949	2.534	2.987	-1.411	-3.237	0.719	3.084	2.13	2.987
TLR3	0.838	3.494	0.205	3.762	1.315	4.669	-0.633	-4.006	0.477	3.342	1.11	4.269
TRIM21	2.927	-2.197	0.871	-1.961	4.113	-2.197	-2.056	1.961	1.186	-1.961	3.242	-2.197
USP18	5.873	-2.789	2.606	-2.789	6.818	-3.121	-3.267	2.789	0.946	-2.207	4.213	-3.121
ZBP1	NA	NA	2.919	2	5.471	2	-1.094	-2	1.458	2	2.552	1.342

Supplemental Figure 4

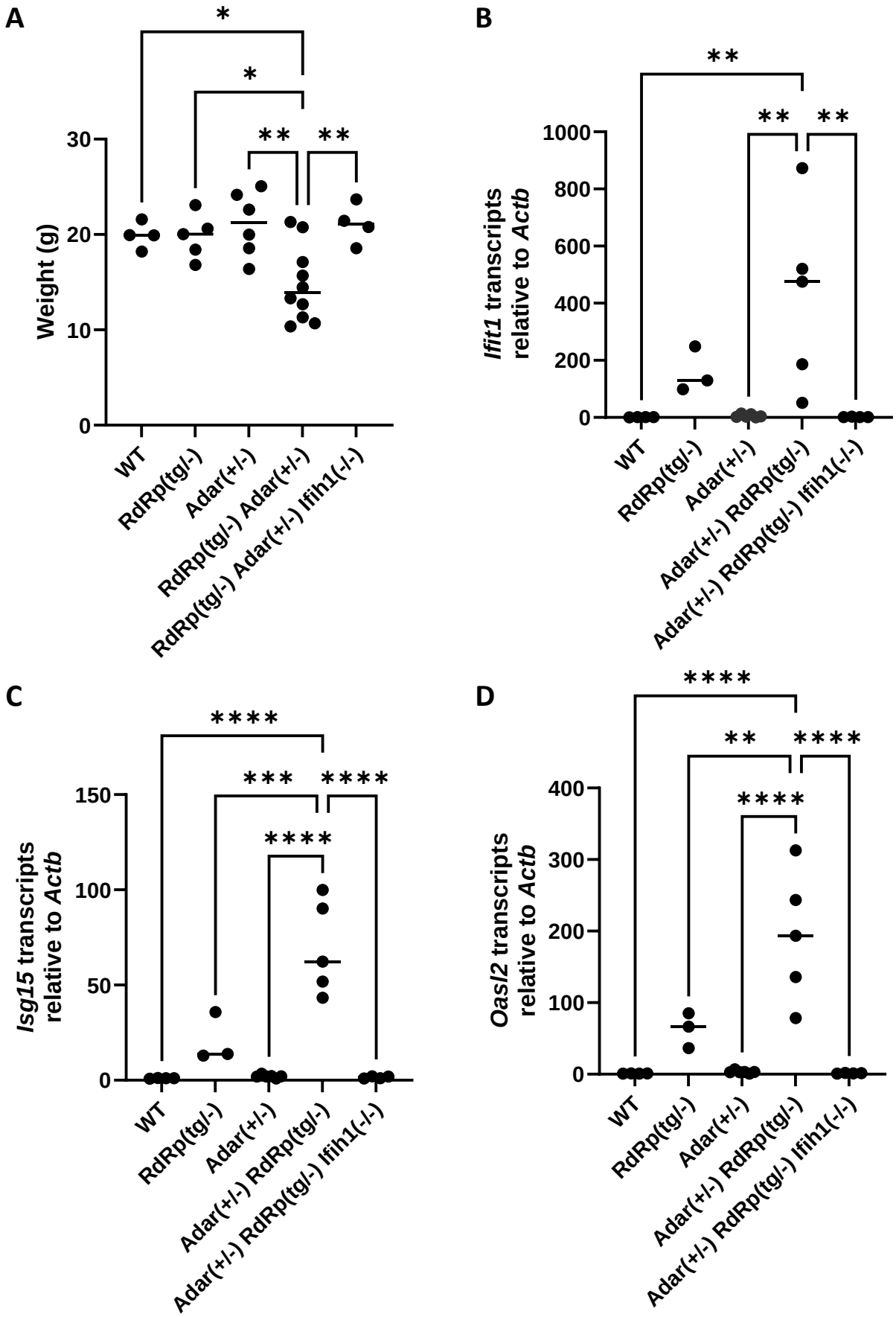

Supplemental Figure 5

Diseases or Functions Annotation	WT vs. RdRp$^{tg/-}$	WT vs. Adar$^{+/-}$	WT vs. RdRp$^{tg/-}$ Adar$^{+/-}$	RdRp$^{tg/-}$ vs. Adar$^{+/-}$	RdRp$^{tg/-}$ vs. RdRp$^{tg/-}$ Adar$^{+/-}$	Adar$^{+/-}$ vs. RdRp$^{tg/-}$ Adar$^{+/-}$
Activation of cells	2.339	1.88	2.069	-2.262	1.501	2.154
Activation of macrophages	1.803	1.282	2.145	-1.803	1.898	1.633
Activation of myeloid cells	1.472	0.943	2.084	-1.472	2.095	1.698
Activation of phagocytes	1.469	0.938	1.765	-1.469	2.095	1.795
Adhesion of blood cells	1.989	NA	2.637	NA	2.132	2.025
Antigen presentation	2.414	NA	2.414	NA	NA	2.414
Antigen presentation by cells	2	NA	2	NA	NA	2
Antimicrobial response	2.787	2.406	2.792	-2.947	NA	2.792
Antiviral response	2.787	2.406	2.792	-2.947	NA	2.792
Antiviral response of cells	2.219	1.982	1.31	-2.219	NA	1.31
Apoptosis	0.916	0.197	1.616	-0.696	1.157	2.443
Apoptosis of tumor cell lines	NA	NA	1.173	-0.889	NA	2.09
Autophagy of cells	2.072	NA	1.363	-1.502	1.095	1.152
Cell cycle progression	2.961	NA	2.195	-2.809	NA	2.448
Cell death of epithelial cells	NA	NA	1.966	NA	NA	2.68
Cell death of tumor cell lines	1.044	NA	1.396	-1.388	NA	2.158
Cell movement of leukocytes	2.904	NA	1.35	-2.394	1.501	1.387
Cell movement of monocytes	2.185	NA	2.083	NA	1.571	2.083
Cell movement of T lymphocytes	2.544	1.948	1.072	-1.824	1.645	1.072
Cellular homeostasis	1.314	1.026	2.089	-1.662	0.957	1.356
Cellular infiltration	2.619	NA	0.842	-1.692	1.402	1.042
Cellular infiltration by leukocytes	2.696	2.342	1.081	-2.13	1.481	1.294
Cellular infiltration by lymphocytes	2.187	NA	0.201	-1.507	0.692	0.201
Cellular infiltration by myeloid cells	1.878	2.091	0.83	NA	0.935	0.791
Contact growth inhibition	2.232	NA	2.467	-2.052	NA	2.467
Contact growth inhibition of tumor	NA	NA	2.022	-1.49	NA	2.022
Coordination	NA	NA	NA	NA	-2.401	NA
Cytostasis	2.442	NA	2.742	-2.522	NA	2.742
Cytostasis of tumor cell lines	1.972	1.451	NA	-1.762	NA	2.232
Cytotoxicity of cytotoxic T cells	2.439	NA	2.635	-1.988	NA	2.438
Cytotoxicity of lymphocytes	2.794	NA	2.605	-2.048	NA	2.412
Cytotoxicity of T lymphocytes	NA	NA	2.332	-1.583	NA	2.112
Degradation of DNA	NA	NA	2.781	NA	NA	2.781
Demyelination of nerves	NA	NA	1.798	NA	2.057	1.541
Differentiation of T lymphocytes	1.859	NA	1.227	-2.1	NA	0.815
Elimination of cells	NA	NA	2.2	NA	1.964	2.2
Encephalitis	-1.515	-1	-2.141	NA	-1.405	-2.141
Endocytosis	2.6	NA	NA	NA	NA	0.566
Fragmentation of DNA	NA	NA	2.598	NA	NA	2.598
Hematologic cancer	NA	NA	-2.752	NA	NA	-2.752
Hematologic cancer of cells	NA	NA	-2.396	NA	NA	-2.396
Hematopoietic neoplasm	NA	NA	-2.032	NA	NA	-2.032
Immune response of brain	-1.745	NA	-2.311	1.992	NA	-2.311
Immune response of cells	3.924	3.1	2.981	-3.066	NA	2.445
Immune response of leukocytes	2.415	1.981	0.755	-1.218	1.004	0.08
Infection by Flaviviridae	-1.732	-1.732	-2	1.732	NA	-2
Infection by Herpesviridae	NA	NA	-2.187	NA	NA	-2.187
Infection by RNA virus	-1.879	-2.019	-2.719	2.088	-1.388	-2.745
Infection of cells	-1.152	NA	-2.341	1.417	-1.2	-2.371
Infection of kidney cell lines	-1.651	-1.337	-2.093	1.651	NA	-2.291
Infection of mammalia	-3.48	-2.662	-3.452	3.388	-1.445	-3.207
Infiltration by T lymphocytes	2.187	NA	0.052	-1.507	0.842	0.052
Inflammation of absolute anatomic	-1.386	-0.851	-2.132	1.358	-0.958	-2.132
Inflammation of organ	-1.311	-0.729	-2.222	1.29	-0.76	-2.173
Inhibition of lymphocytes	NA	NA	2.172	NA	NA	2.172
Inhibition of RNA virus	1.974	NA	2.196	-1.974	NA	1.568
Inhibition of virus	NA	NA	2.415	-2.211	NA	1.848
Innate immune response	2.63	2.219	3.43	-3.132	2.8	3.43
Leukocyte migration	2.991	NA	1.565	-2.488	1.505	1.326
Lymphatic system tumor	NA	NA	-2.592	NA	NA	-2.592
Lymphocyte migration	2.721	2.144	0.753	-2.044	1.211	0.753
Lymphocytic cancer	NA	NA	-2.593	NA	NA	-2.593
Lymphocytic neoplasm	NA	NA	-2.593	NA	NA	-2.593
Lymphohematopoietic cancer	NA	NA	-2.752	NA	NA	-2.752
Lymphohematopoietic neoplasia	NA	NA	-2.032	NA	NA	-2.032
Lymphoid cancer	NA	NA	-2.593	NA	NA	-2.593
Lymphoreticular neoplasm	NA	NA	-2.4	NA	NA	-2.4
Migration of cancer cells	1.342	2	0.213	-1.342	0.956	0.508
Migration of cells	3.179	2.898	1.999	-2.573	0.825	1.285
Morbidity or mortality	-2.789	NA	-1.199	NA	0.575	-0.651
Necrosis	1.494	1.476	2.39	-1.714	2.274	2.989
Necrosis of epithelial tissue	NA	NA	1.737	NA	NA	2.346
Neoplasia of blood cells	NA	NA	-2.512	NA	NA	-2.512
Neoplasia of leukocytes	NA	NA	-2.396	NA	NA	-2.396
Neuromuscular disease	2.219	1.982	1.664	-1.982	1.387	1.664
Polarization of blood cells	NA	NA	NA	NA	2	NA
Polarization of cells	NA	1.982	NA	NA	2.219	NA
Production of protein	1.53	1.217	1.148	-2.096	0.485	0.678
Quantity of blood cells	2.217	1.36	0.079	-2.117	0.041	0.653
Quantity of CD8+ T lymphocyte	2.388	2.191	1.721	-2.207	1.461	1.721
Quantity of cytokine	NA	NA	-2.343	NA	NA	-2.154
Quantity of IFNG in blood	-2.183	NA	-2.4	2.183	NA	-2.4
Quantity of MHC Class I on cell surf	2.207	NA	2.207	-1.981	NA	2.207
Recruitment of leukocytes	2.339	2.339	2.156	-1.666	1.812	1.089
Recruitment of T lymphocytes	1.96	1.96	2.199	-1.96	1.996	NA
Replication of Flaviviridae	-2.643	-2.643	-2.988	2.826	-2.275	-2.988
Replication of flavivirus	-1.963	-2.181	-2.181	2.181	-1.939	-2.181
Replication of Hepatitis C virus	-2.335	-2.111	-2.528	2.324	NA	-2.528
Replication of Herpesviridae	-2.132	-2.828	-3.175	2.525	-2.236	-3.175
Replication of Murine herpesvirus 4	-2.236	-2	-2.828	2.236	NA	-2.828
Replication of RNA virus	-2.875	-3.077	-3.617	3.292	-2.304	-3.497
Replication of vesicular stomatitis	-2.679	-2.473	-3.129	2.841	-1.702	-3.129
Replication of viral replicon	-2.818	-3.115	-3.56	3.271	-2.782	-3.56
Replication of virus	-3.082	-3.443	-3.924	3.583	-2.607	-3.812
Response of antigen presenting cel	2.219	NA	1.65	NA	NA	0.799
Response of embryonic cell lines	1.96	NA	2.4	-2.2	NA	2.4
Response of epithelial cell lines	1.969	NA	2.404	-2.207	NA	2.404
Response of kidney cell lines	1.969	NA	2.404	-2.207	NA	2.404
Response of phagocytes	2.207	2.207	NA	-2.207	NA	0.845
Transactivation of RNA	NA	1.961	NA	-2.41	NA	NA
Viral Infection	-3.615	-3.851	-4.1	3.801	-2.583	-3.943
Viral life cycle	NA	NA	-3.683	NA	NA	-3.683

Supplemental Figure 6

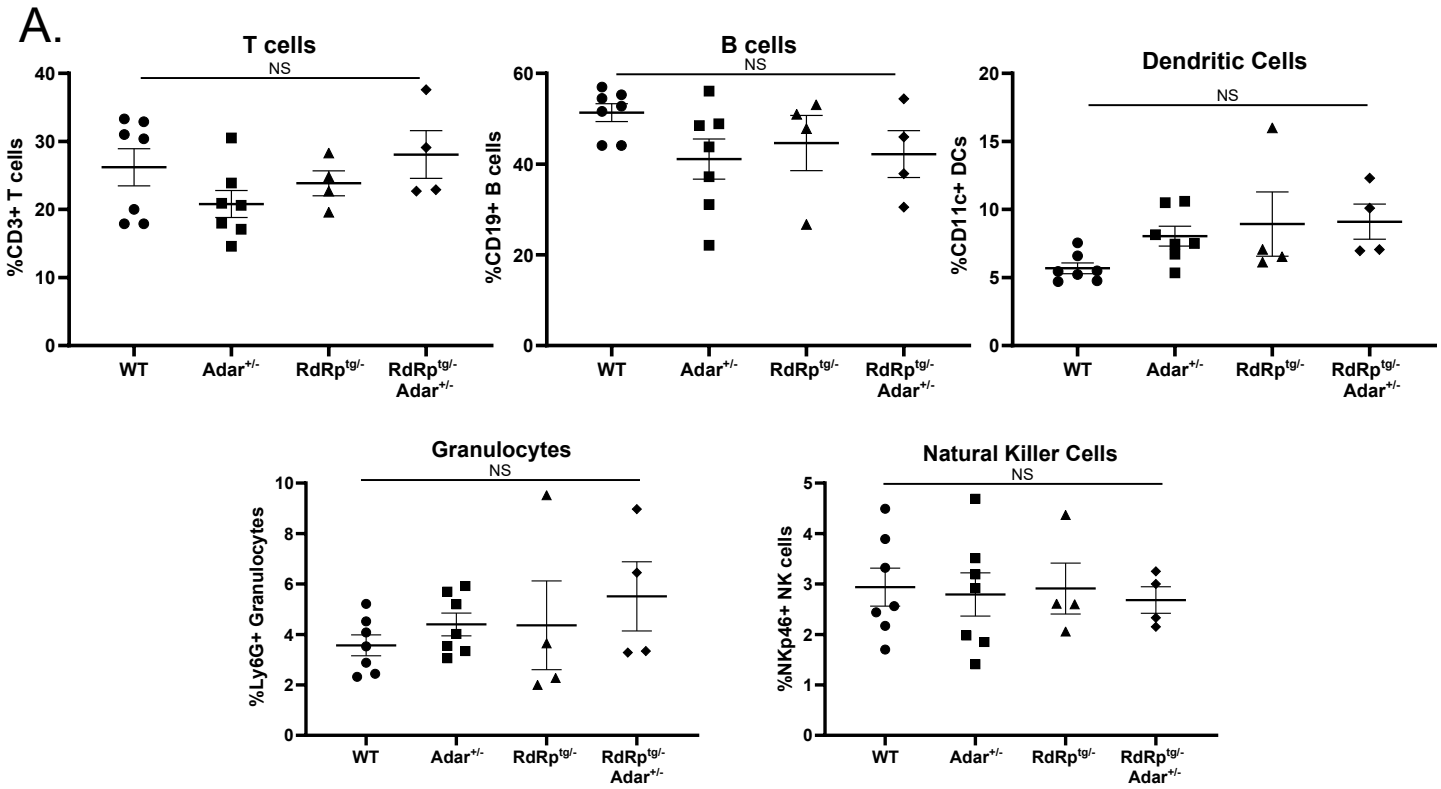

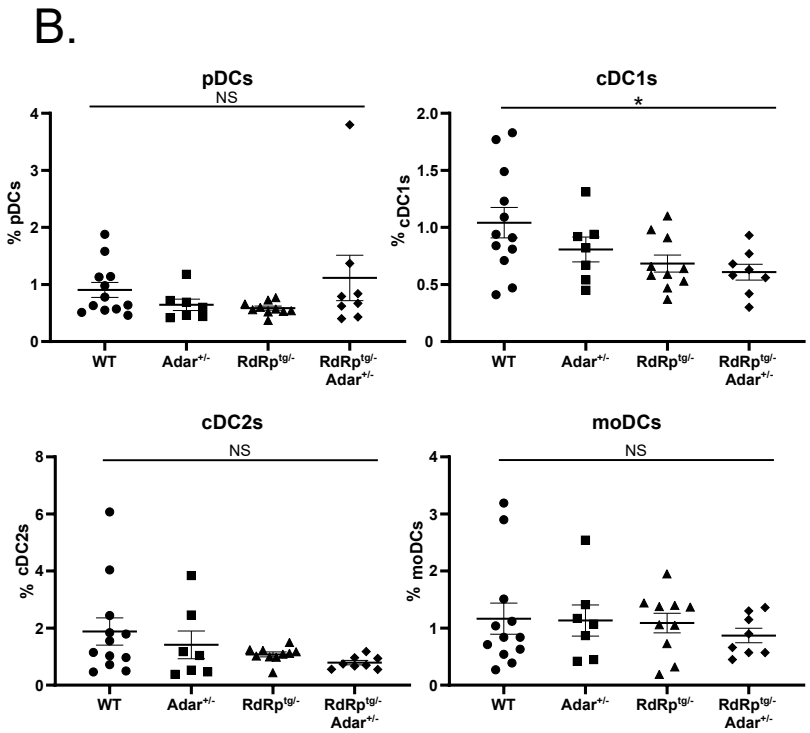

Supplemental Figure 7

	WT vs. RdRp$^{tg/-}$		WT vs. Adar$^{+/-}$		WT vs. RdRp$^{tg/-}$ Adar$^{+/-}$		RdRp$^{tg/-}$ vs. Adar$^{+/-}$		RdRp$^{tg/-}$ vs. Adar$^{+/-}$ RdRp$^{tg/-}$		Adar$^{+/-}$ vs. Adar$^{+/-}$ RdRp$^{tg/-}$	
Diseases or Functions Annotation	**-log(B-H p-value)**	**z-score**	**-log(B-H p-value)**	**z-score**	**-log(B-H p-value)**	**z-score**	**-log(B-H p-value)**	**z-score**	**-log(B-H p-value)**	**z-score**	**-log(B-H p-value)**	**z-score**
Antimicrobial response	0.00000	2.39	1.97E-09	1.455	NaN	NaN	0.00000	-2.39	1.08E-05	NaN	1.21E-12	0.995
Antiviral response	0.00000	2.39	2.77E-11	1.455	NaN	NaN	0.00000	-2.39	2.82E-06	NaN	6.75E-12	0.995
Apoptosis of breast cancer cell lines	NaN	NaN	NaN	NaN	NaN	NaN	NaN	NaN	NaN	NaN	0.00146	2.808
Apoptosis of epithelial cells	NaN	NaN	NaN	NaN	NaN	NaN	NaN	NaN	NaN	NaN	0.00003	2.55
Apoptosis of liver cells	NaN	NaN	NaN	NaN	NaN	NaN	NaN	NaN	NaN	NaN	0.00146	2.169
Cell death of epithelial cells	0.00251	2.414	NaN	NaN	NaN	NaN	NaN	NaN	1.06E-03	0.922	1.41E-05	3.058
Demyelination of nerves	NaN	NaN	NaN	NaN	NaN	NaN	NaN	NaN	0.00001	2.195	NaN	NaN
Differentiation of Th17 cells	NaN	NaN	NaN	NaN	NaN	NaN			NaN	NaN	0.00014	-2.382
Encephalitis	3.09E-04	-1.925	3.72E-07	0.264	NaN	NaN	NaN	NaN	1.09E-04	-1.361	0.00000	-3.488
Experimental autoimmune encephalomyelitis	5.09E-04	-1.639	7.57E-07	0.659	NaN	NaN	1.45E-06	1.881	1.66E-04	-1.37	0.00000	-3.326
Inflammation of absolute anatomical region	8.46E-06	-1.905	5.51E-08	-0.527	NaN	NaN	1.39E-07	1.365	0.00002	-2.537	0.00000	-3.351
Inflammation of organ	3.08E-05	-1.264	1.75E-07	0.255	NaN	NaN	1.71E-07	1.078	0.00001	-2.346	0.00000	-2.881
Inhibition of cells	NaN	NaN	NaN	NaN	NaN	NaN	NaN	NaN	NaN	NaN	0.00142	2.166
Maturation of phagocytes	NaN	NaN	2.29E-03	-0.169	NaN	NaN	0.00074	-2.183	NaN	NaN	5.47E-04	0.891
Necrosis	8.48E-03	1.117	NaN	NaN	NaN	NaN	NaN	NaN	0.00160	2.156	0.00004	2.291
Necrosis of epithelial tissue	NaN	NaN	NaN	NaN	NaN	NaN	NaN	NaN	1.36E-04	1.014	0.00000	2.072
Neuronal cell death	NaN	NaN	NaN	NaN	NaN	NaN	NaN	NaN	0.00476	2.302	0.00006	2.309
Proliferation of antigen presenting cells	NaN	NaN	NaN	NaN	NaN	NaN	2.26E-03	-0.865	3.64E-03	NaN	0.00014	2.201
Proliferation of blood cells	0.00421	2.084	NaN	NaN	NaN	NaN	NaN	NaN	9.98E-04	0.317	8.85E-06	0.535
Proliferation of immune cells	0.00429	2.084	NaN	NaN	NaN	NaN	NaN	NaN	9.14E-04	0.358	1.70E-05	0.808
Quantity of blood cells	0.00064	2.383	NaN	NaN	NaN	NaN	0.00193	-2.021	1.63E-04	0.487	2.79E-06	0.67
Quantity of IL-12 in blood	0.00002	-2	6.62E-03	NaN	NaN	NaN	0.00002	2	NaN	NaN	0.00007	-2
Quantity of interleukin	NaN	NaN	NaN	NaN	NaN	NaN	NaN	NaN	NaN	NaN	0.00064	-2
Quantity of leukocytes	0.00046	2.295	NaN	NaN	NaN	NaN	1.60E-03	-1.906	1.02E-04	0.167	9.96E-07	0.336
Quantity of phagocytes	0.00104	2.191	NaN	NaN	NaN	NaN	2.21E-03	-1.544	2.25E-05	-0.125	5.80E-05	-0.102
Quantity of protein in blood	0.00769	-2.909	NaN	NaN	NaN	NaN	0.00034	2.088	NaN	NaN	6.48E-04	-1.717
Rheumatic Disease	0.00000	-2.219	7.94E-05	-1	NaN	NaN	7.74E-07	1.179	3.07E-05	-0.503	2.99E-08	-1.157

Supplemental Figure 8

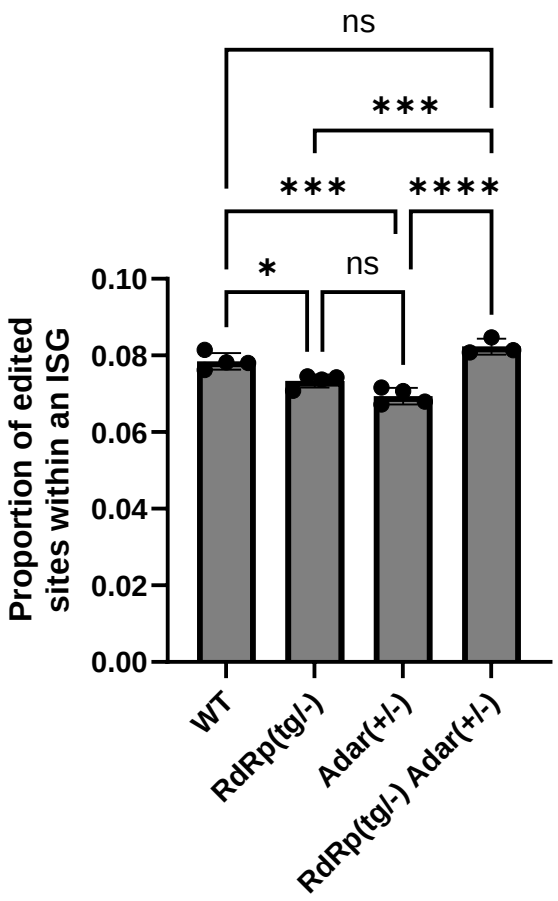

Supplemental Figure 9

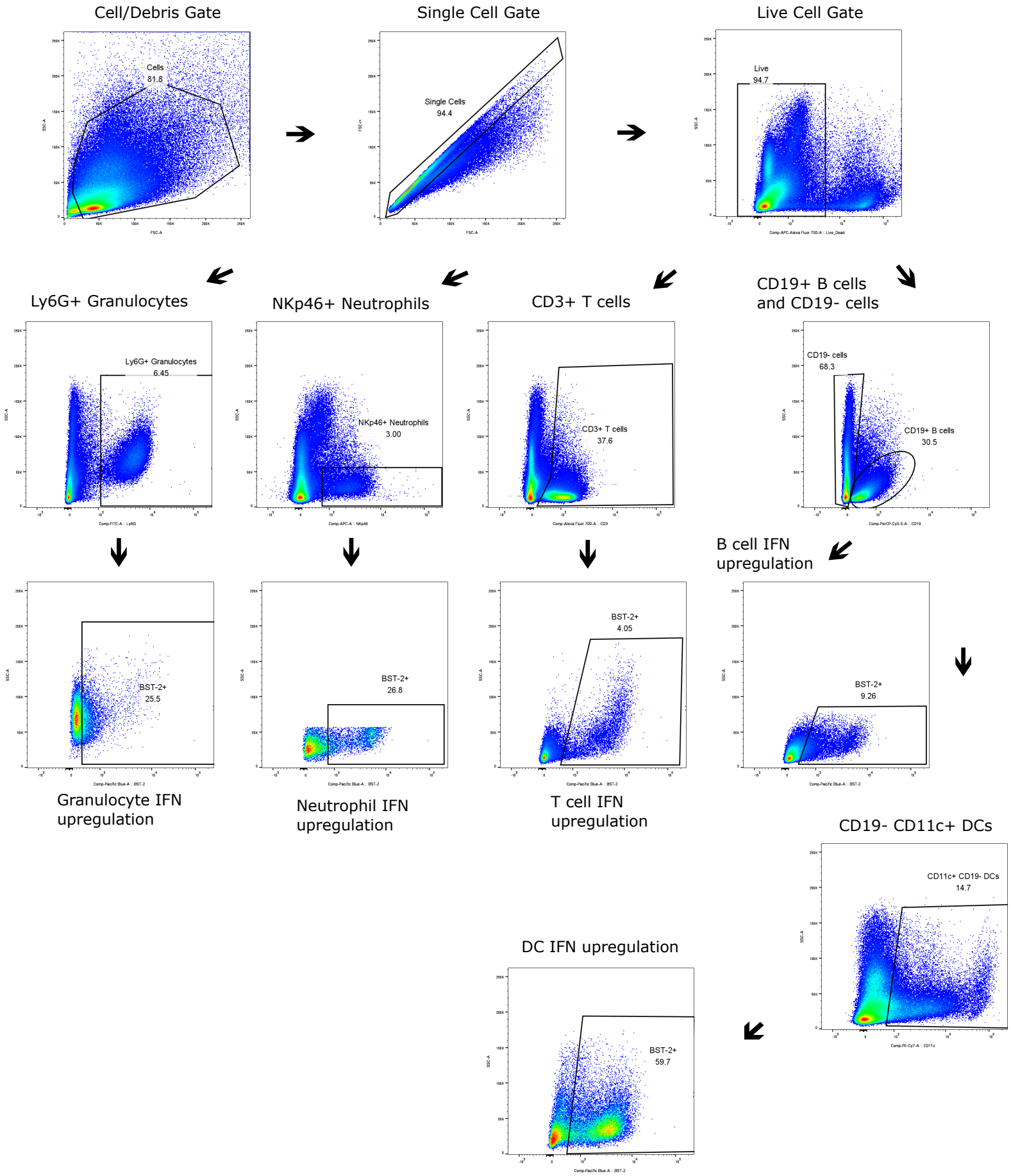

Supplemental Figure 10

B cells

Cell/Debris Gate

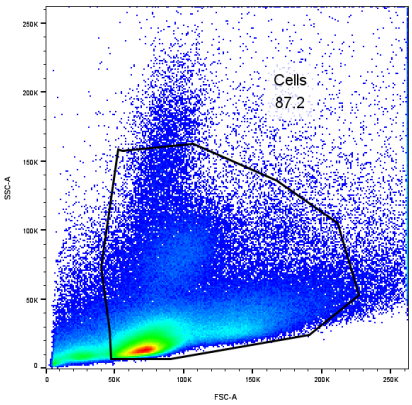

Single Cell Gate

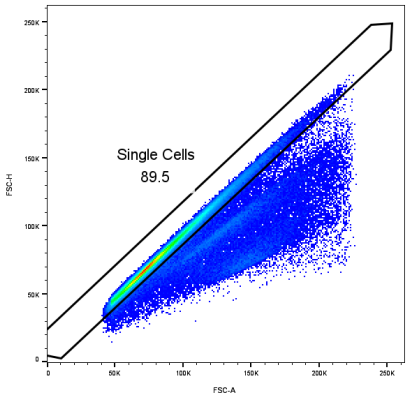

Live/Dead Gate

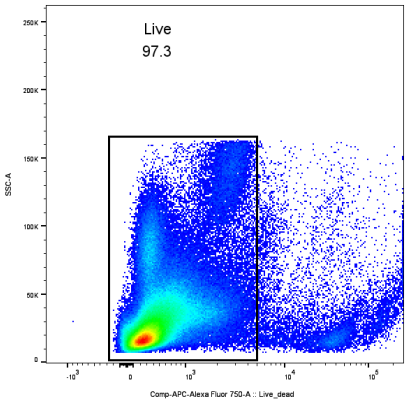

CD19lo CD138+
Plasma Cell Gate

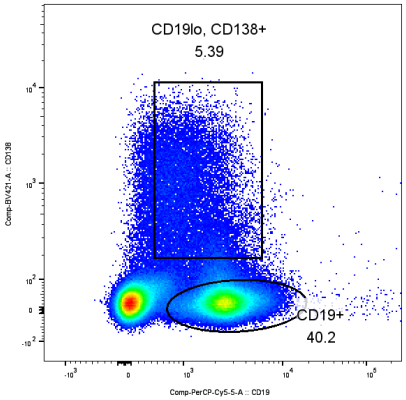

CD19 high Fas+ GL-7+
Germinal Center B cell Gate

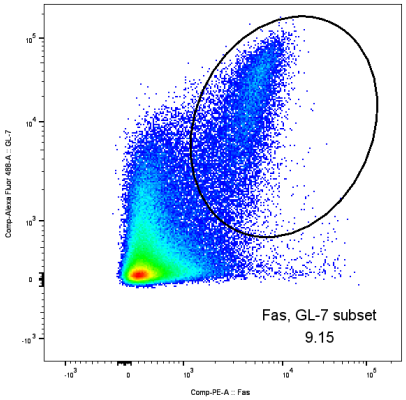

T cells

Cells/Debris Gate

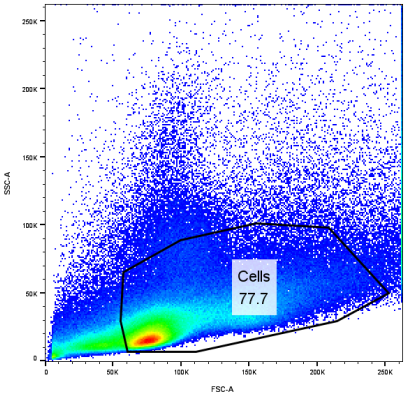

Single Cell Gate

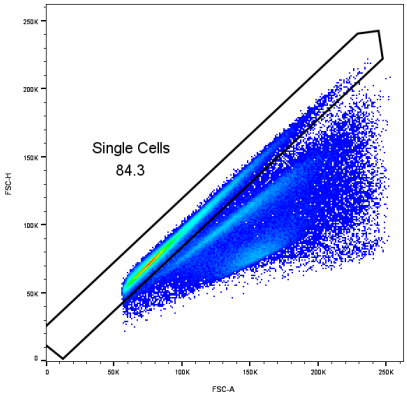

Live/Dead Gate

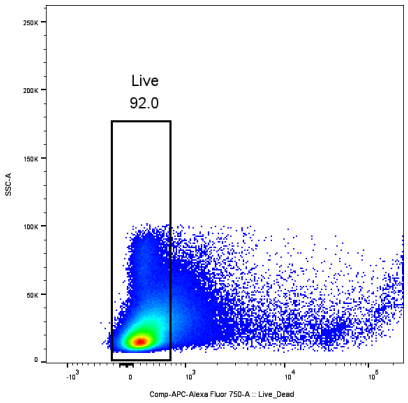

TCRb+ CD4+ T cell
Gate

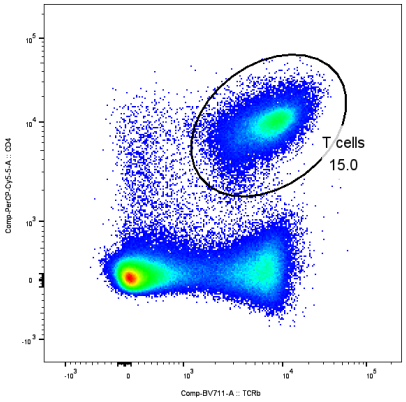

CXCR5+ PD-1+
Tfh Gate

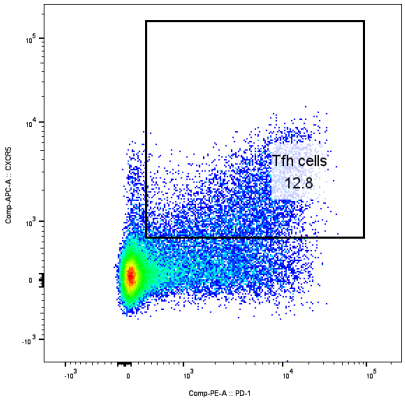

Supplemental Figure 11

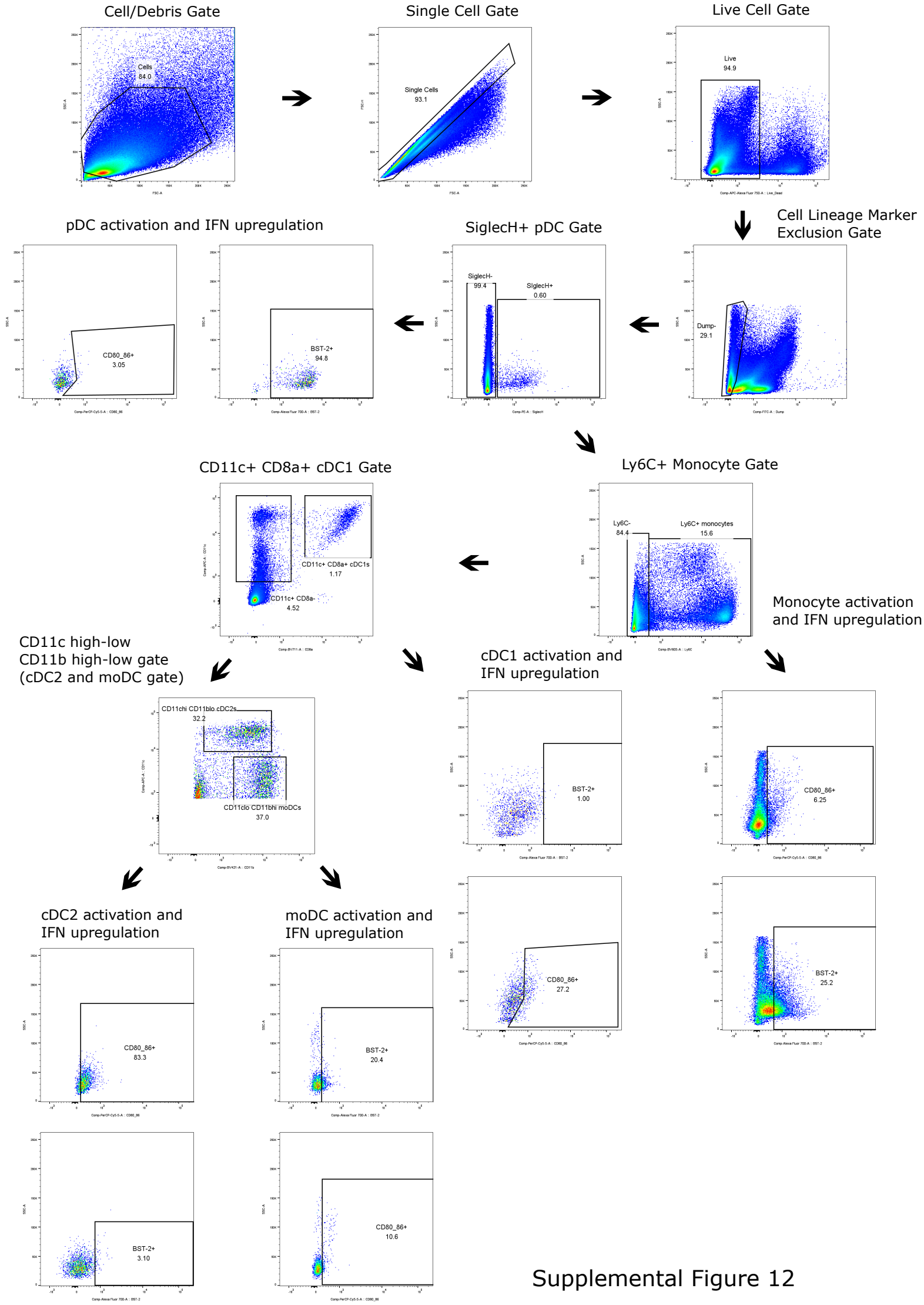

Supplemental Figure 12

Cell/Debris Gate

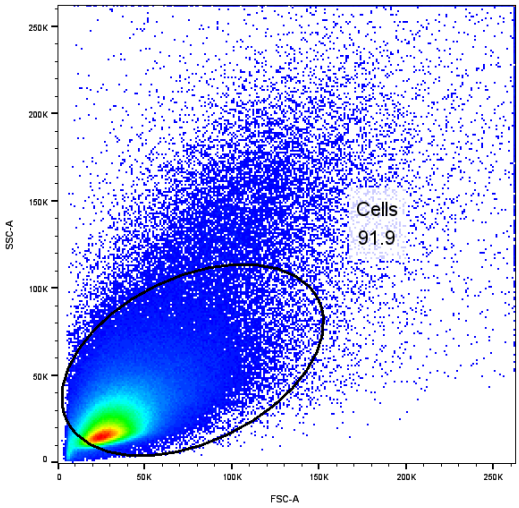

Single Cell Gate

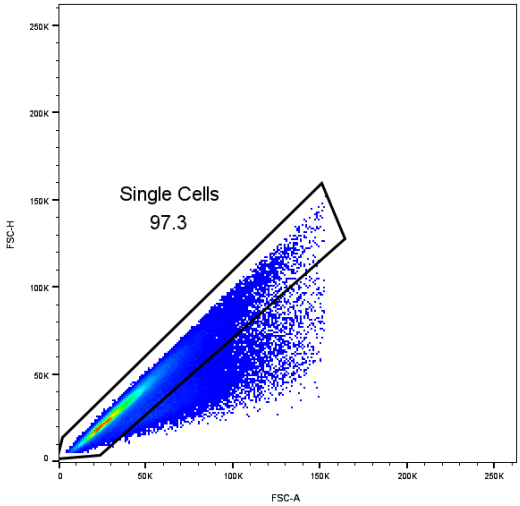

Live Cell Gate

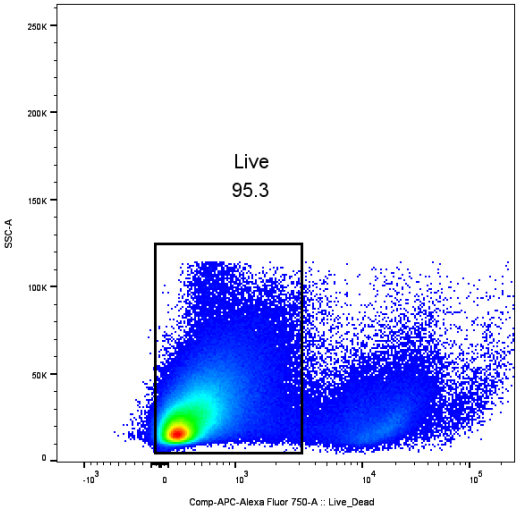

CD4+ FoxP3+
Treg gate

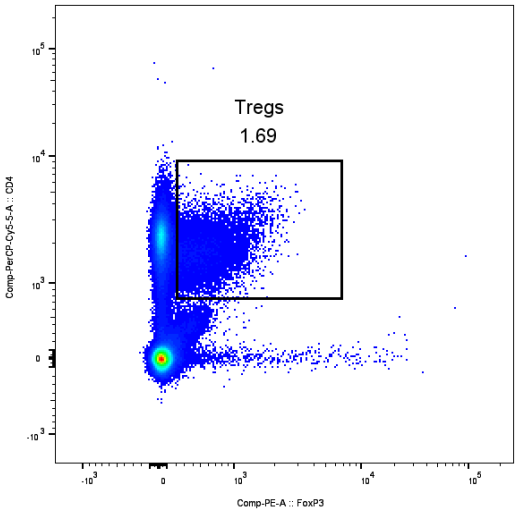

Effector Treg (CD62L-CD44+)
and Naiive Treg (CD62L+CD44-) Gate

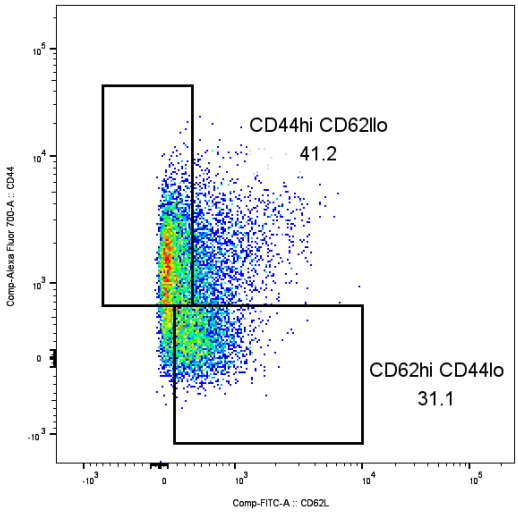

Supplemental Figure 13